arXiv:2605.15760v1 [cs.CV] 15 May 2026

Learn2Splat: Extending the Horizon of Learned 3DGS Optimization

Naama Pearl[1⋆], Stefano Esposito[1⋆], Haofei Xu[1,2], Amit Peleg[1], Patricia Gschoßmann[1], Lorenzo Porzi[3], Peter Kontschieder[3], Gerard Pons-Moll[1], and Andreas Geiger[1]

[1] University of Tübingen, Tübingen AI Center
[2] ETH Zurich
[3] Meta Reality Labs

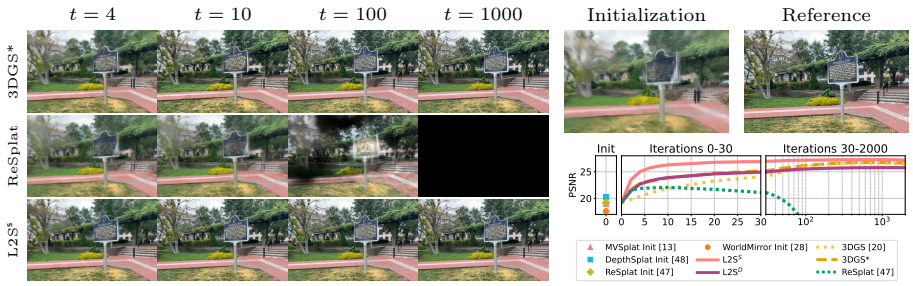


Fig. 1: Learn2Splat (L2S) is a learned optimizer for 3DGS that reaches higher reconstruction quality in early stages, while remaining effective across long optimization horizons. Prior learned optimizers (LOs) [14, 29, 47] rely on learning rate (LR) schedules or time encodings to converge, limiting them to short or predefined number of iterations; beyond these, reconstruction can degrade (Sec. 5.2). Learn2Splat maintains performance across long optimization horizons through a combination of meta training scheme and architectural modifications (Sec. 4). Our learned optimizer can work for both sparse SfM initialization and dense feed-forward initialization. Although trained to reconstruct low-resolution scenes, it zero-shot generalizes to other datasets and resolutions. Here, we show high-resolution (zero-shot) sparse-view reconstructions on DL3DV [26], comparing to ReSplat [47], 3DGS [20], and its tuned variant (3DGS*).

Abstract. 3D Gaussian Splatting (3DGS) optimization is most commonly performed using standard optimizers (Adam, SGD). While stable across diverse scenes, standard optimizers are general-purpose and not tailored to the structure of the problem. In particular, they produce independent parameter updates that do not capture the structural and spatial relationships within a scene, leading to inefficient optimization and slow convergence. Recent works introduced learned optimizers that predict correlated updates informed by inter-parameter and inter-Gaussian dependencies. However, these methods are trained for a fixed number of

⋆ Equal contribution.

optimization iterations and rely on manually scheduled learning rates to avoid degradation. In this paper, we introduce a learned optimizer for 3DGS that avoids degradation over extended optimization horizons without auxiliary mechanisms. To enable this, we propose a meta-learning scheme that extends the optimization horizon via a checkpoint buffer and an optimizer rollout strategy, combined with an architecture that encodes gradient scale information in its latent states. Results show improved early novel view synthesis quality while remaining stable over long horizons, with zero-shot generalization to unseen reconstruction settings. To support our findings, we introduce the first unified framework for training and evaluating both learned and conventional optimizers across sparse and dense view settings. Code and models will be released publicly. Our project page is available at https://naamapearl.github.io/learn2splat.

Keywords: Gaussian Splatting, Learning to Optimize, View Synthesis

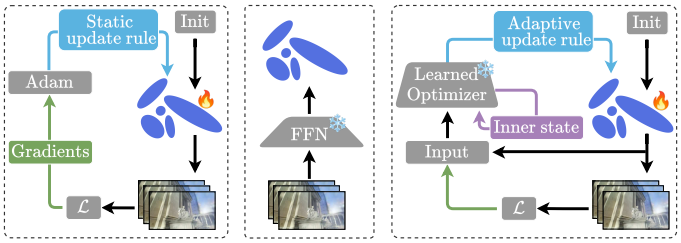
1 Introduction

Recent advances in 3D scene reconstruction and novel view synthesis (NVS) have led to increasingly efficient and expressive representations. Among them, 3D Gaussian Splatting (3DGS) [20] represents scenes as a set of 3D Gaussians rendered via efficient differentiable rasterization.

However, 3DGS relies on per-scene optimization that typically runs for thousands of iterations for every new scene (Fig. 2a). General-purpose optimizers such as Adam [22] and SGD [21,38], while robust and widely used, are not specifically tailored to the 3DGS loss landscape and training dynamics. Their updates are applied independently to each parameter and each Gaussian, and they do not leverage priors about scene geometry, appearance, or parameter dynamics.

A natural attempt to bypass iterative optimization is to directly predict Gaussian parameters from input images using feed-forward networks (FFN) [10, 13, 19, 27, 28, 47, 48]. These approaches typically operate in sparse-view settings, predicting a set of Gaussians for each input view, commonly one Gaussian per pixel. However, capturing fine-grained geometric and photometric details in a single forward pass often exceeds the representational capacity of current architectures. Consequently, to match the quality of per-scene optimization methods, these models typically require additional scene-specific, iterative fine-tuning. In this work, we refer to this type of model as *learned initializers*, as their predicted set of Gaussians can serve as initialization to any 3DGS optimization strategy.

A complementary strategy is to preserve the iterative optimization paradigm, replacing standard optimizers with a *meta-learned optimizer* that predicts parameter updates (Fig. 2c). This general-purpose meta-learning paradigm [3, 43] follows the structure of gradient-based optimization, operating on the gradients of a predefined loss function. These gradients are often pre-processed through normalization [43], logarithmic scaling [3], or moment averaging [5] before being passed to the optimizer. This enables the optimizer to exploit shared patterns across training episodes and adapt dynamically to each scene, supporting flex-



(a) Standard optimizer **(b)** FFN **(c)** Learned optimizer

Fig. 2: 3DGS Optimization Paradigms. (a) In per-scene optimization (Section 3.2), the scene representation is learned through iterative updates based on loss evaluation, gradient backpropagation, and standard optimizer rules. (b) In feed-forward networks (FFN), the scene representation is predicted in a single forward pass using a pre-trained model. (c) Learned optimizers (Section 3.3) iteratively update the scene representation with a frozen pre-trained model that predicts update steps from input signals such as rendering errors or loss gradients.

ible, data-driven update behaviors that can outperform hand-crafted optimization rules. Throughout this work, we use the term *learned optimizer* to refer to any learning-based iterative method updating parameters of another model.

Recent works [14,29,47] have begun exploring learned optimization strategies within the 3DGS framework. While these approaches demonstrate that learned refinement can accelerate optimization and enhance visual fidelity, they saturate early or even diverge outside their trained optimization horizon. We argue that a desirable property of any learned optimizer is long-horizon robustness: as the loss decreases, the optimizer's predicted updates should naturally vanish. Existing methods rely on auxiliary mechanisms such as learning rate schedules and are tied to a short, predefined number of iterations. In contrast, our architecture and meta-learning scheme learns to decay updates as optimization progresses.

To this end we propose Learn2Splat, a long-horizon learned optimizer for 3D Gaussian Splatting. Unlike prior learned optimizers, Learn2Splat remains effective across long optimization trajectories and achieves better reconstruction in early stages. Our architecture enables the optimizer to encode the magnitude of the input gradients (Sec. 4.2), while our loss formulation provides effective supervision on the predicted updates (Sec. 4.1). Furthermore, our training approach integrates a *checkpoint buffer* (CB) and an *optimizer rollout* (OR) mechanism (Sec. 4.3) that expose the network to diverse optimization states and improve its performance across different optimization stages (see Fig. 1). To show that our architecture and meta-learning scheme are not tied to a specific initialization or view setting, we train Learn2Splat in both sparse and dense view settings, using an FFN and SfM points [2] initialization, respectively. For each setting, we evaluate zero-shot generalization to unseen resolutions and datasets, including RealEstate10K [52], LLFF [35], DTU [1], and MipNeRF360 [4]. Additionally, we probe cross-setting behavior by applying each trained model outside its training regime. To support this study, we introduce the first unified framework for 3DGS optimization that supports both learned and standard optimizers.

2 Related Work

Meta-Learning and Learned Optimizers. Standard optimizers such as SGD [38] and Adam [22] are general-purpose methods that require hyperparameter tuning. Meta-learning [11], by contrast, seeks to learn optimizers that generalize across related tasks by encoding priors about the optimization process itself. Early work on learning update rules dates back to [6, 7], while [3] introduced the first deep learned optimizer for tasks such as MNIST classification and style transfer. Subsequent research [33, 34, 43] investigated training stability and scalability, proposing strategies for more effective meta-optimization. Despite these advancements, general learned optimizers are usually trained on an immense amount of tasks for a rather mild speed-up. Several works address 3D learning tasks. For instance, for 3D rigid body motion estimation from RGB-D inputs, [31] parametrized the components of a classical optimization algorithm. For 3D human model fitting, [15] learns a function to predict vertex position updates; [46] learns to predict parameter updates for faces. Other works [16, 17] address NVS by updating multiplane image representations using a learned gradient descent optimizer. In this paper, we train a learned optimizer for NVS with 3DGS such that it generalizes across datasets and settings.

Standard 3DGS Optimization. 3D Gaussian Splatting (3DGS) [20] represents scenes as a collection of 3D Gaussian primitives, which enables real-time and photo-realistic novel view synthesis. However, existing 3DGS approaches still depend on expensive per-scene optimization using standard gradient-based optimizers, often requiring minutes to hours of computation for a single scene. To speed up the per-scene optimization process, Taming 3DGS [32] and [9] improve the densification process to make the primitive count deterministic and implement several low-level optimizations for faster convergence. ScaffoldGS [30] proposes an anchor-based primitives distribution strongly increasing training efficiency on dense scenes. EDGS [24] suggests that densification may be unnecessary for high-quality reconstruction given strong initialization. Second-order optimization methods [18, 25, 50] are also proposed to accelerate convergence. However, existing optimization methods usually involve heuristics and hyperparameter tuning, which is time-consuming and limits their scalability.

Single-Step Feed-Forward 3DGS. To address the limitations of per-scene optimization, feed-forward 3DGS models [10, 39] have been proposed to directly predict a set of Gaussians from input images in a single feed-forward inference. Significant progress has been made recently and the performance on standard benchmarks has been steadily improved [13, 19, 27, 28, 41, 42, 48]. However, their reconstruction quality and generalization ability are inherently constrained by the single-step feed-forward inference [47]. Further improving the quality and robustness of feed-forward models remains to be a significant challenge.

Learned Optimizers for 3DGS. Recent works have begun exploring learned optimization for 3DGS. G3R [14] and QuickSplat [29] employ gradient-conditioned networks that predict parameter updates from gradients of the rendering

loss. In particular, G3R [14] uses a sparse 3D CNN to infer update steps for a Gaussian scene representation conditioned on Gaussian parameters and their gradients wrt. input views. QuickSplat [29] focuses on surface reconstruction rather than view synthesis, combining an initialization network with interleaved optimization and densification to refine 3DGS scenes from SfM initialization. ReSplat [47], in contrast, predicts updates from rendering errors rather than gradients, and performs well under sparse-view conditions. The concurrent work GIFSplat [12] shares similar idea with ReSplat, but focuses on pose-free settings.

Despite their differences, these learned optimizers share key limitations: they rely on meta training protocols tied to fixed training horizons. Consequently, they may exhibit performance saturation or degradation beyond the number of training iterations they are trained on. For instance, QuickSplat applies only five learned steps followed by 2000 regular gradient updates to improve reconstruction quality. G3R is trained for 24 steps and evaluated for up to 100 iterations using a LR schedule. ReSplat, trained for four steps, deteriorates beyond roughly ten iterations. In contrast, we propose a meta-learning framework that adapts to long horizons in 3DGS optimization, resulting in a stable learned optimizer. Furthermore, our learned optimizer works for initialization from sparse SfM and dense feed-forward reconstructions.

3 Preliminaries

In this section, we review the fundamentals of the 3DGS framework (Section 3.1), standard optimizers (Section 3.2) and learned optimizers (Section 3.3) in 3DGS. A summary of the notation is provided in the supp. mat.

3.1 3D Gaussian Splatting

The goal of NVS is to generate novel views from a set of training images of a scene. For a given scene, the training data consists of a set of views $\mathcal{V} = \{\mathcal{V}_i\}_{i=1}^{N}$, each includes the RGB image $\mathbf{I}_i$, the corresponding intrinsic matrix $\mathbf{K}_i$, a translation vector $\mathbf{t}_i$ and a rotation matrix $\mathbf{R}_i$.

3DGS models the 3D world as a set of G 3D Gaussians $\boldsymbol{\mathcal{G}} = \{\boldsymbol{\mathcal{G}}_m\}_{m=1}^{G}$. Each Gaussian $\boldsymbol{\mathcal{G}}_m$ is parametrized by its center $\mathbf{p}_m \in \mathbb{R}^3$, a rotation represented as a quaternion $\mathbf{q}_m \in \mathbb{R}^4$ and a scaling vector $\mathbf{s}_m \in \mathbb{R}^3$. The contribution of each Gaussian in 3D space is determined by an opacity value $\alpha_m \in [0, 1]$, and its color is defined by a set of spherical harmonics coefficients $\mathbf{SH}_m \in \mathbb{R}^{d\times 3}$. For simplicity, we refer to the set of Gaussians as a matrix $\boldsymbol{\mathcal{G}} \in \mathbb{R}^{G\times p}$, where p is the number of parameters in each Gaussian. We denote by $\tilde{\mathbf{I}}_i(\boldsymbol{\mathcal{G}})$ the rendered image of the 3D Gaussians $\boldsymbol{\mathcal{G}}$ given a viewpoint $\mathcal{V}_i$. The supplementary material contains the full rendering derivation. The general optimization problem of 3DGS is to fit the Gaussian parameters to the scene by minimizing a loss term:

$$\underset{\boldsymbol{\mathcal{G}}}{\operatorname{argmin}} \ \frac{1}{N}\sum_{i=1}^{N} \mathcal{L}(\mathbf{I}_i, \tilde{\mathbf{I}}_i(\boldsymbol{\mathcal{G}})) \tag{1}$$

where $\mathcal{L}(\mathbf{I}_i, \tilde{\mathbf{I}}_i(\boldsymbol{\mathcal{G}}))$ measures the difference between the target image $\mathbf{I}_i$ and the rendered image $\tilde{\mathbf{I}}_i(\boldsymbol{\mathcal{G}})$.

3.2 Standard Optimizers

In standard 3DGS [20], gradient-based optimizers update the Gaussian parameters iteratively for each scene (Fig. 2a). At each iteration t, a set of training views is sampled, and the gradient of the loss wrt. the current Gaussian parameters is computed. For brevity, we denote this gradient as

$$\nabla_{\boldsymbol{\mathcal{G}}_t} = \nabla_{\boldsymbol{\mathcal{G}}_t} \mathcal{L}(\mathbf{I}, \tilde{\mathbf{I}}(\boldsymbol{\mathcal{G}}_t)) \tag{2}$$

The loss may be computed from renderings of multiple views, but for clarity, we omit the view indices in the notation. The update rule for a general optimizer can then be

$$\boldsymbol{\mathcal{G}}_{t+1} = \boldsymbol{\mathcal{G}}_t - \eta_t f\left(\nabla_{\boldsymbol{\mathcal{G}}_t}\right) \tag{3}$$

where $f(\cdot)$ defines a specific optimizer (e.g. SGD or Adam) and a LR η_t scales the updates, and may vary over iterations. The Adam optimizer, for example, adaptively rescales each parameter's gradient using first- and second-moment estimates (See sup. mat.).

Although originally designed for neural network training, Adam performs robustly in 3DGS optimization. However, optimal performance requires carefully tuned LR or schedulers for different parameter subsets due to varying parameter scales and their contributions to the rendered output. Despite this, with an appropriate LR, Adam's first-order updates produce a conservative yet reliable optimization trajectory for each Gaussian parameter. A more detailed analysis of Adam's behavior and per-parameter contributions is provided in the sup. mat.

3.3 Learned Optimizers

A standard optimizer f can be replaced by a learned optimizer $f_{\boldsymbol{\theta}}$, a neural network parameterized by $\boldsymbol{\theta}$ and trained via meta-learning (Fig. 2c). Meta-learning consists of two nested updates. The *inner loop* updates the scene-specific Gaussian parameters using the current parameters of the optimizer $\boldsymbol{\theta}_{t_{\text{meta}}}$:

$$\boldsymbol{\mathcal{G}}_{t+1} = \boldsymbol{\mathcal{G}}_t - f_{\boldsymbol{\theta}_{t_{\text{meta}}}}\left(\nabla_{\boldsymbol{\mathcal{G}}_t}, \boldsymbol{\mathcal{G}}_t\right) \tag{4}$$

The *meta loop* updates the parameters of the optimizer based on the performance of the inner updates, measured by $\mathcal{L}_{\text{meta}}$, across scenes and reconstruction states:

$$\boldsymbol{\theta}_{t_{\text{meta}}+1} = \boldsymbol{\theta}_{t_{\text{meta}}} - \eta_{t_{\text{meta}}} \nabla_{\boldsymbol{\theta}_{t_{\text{meta}}}} \mathcal{L}_{\text{meta}} \tag{5}$$

Due to its learnable nature, a learned optimizer can leverage the structural properties of the underlying representation to produce updates that are more adaptive and informative. Note that the inputs to the learned optimizer may include not only the gradients of the optimized parameters but also other useful signals defined by the specific method, such as the current primitives state, quantities measuring rendering error, or other higher-level contextual features.

4 Method

This section outlines our Learn2Splat framework, its architecture and meta-learning approach. We first introduce the general meta-learning formulation (Section 4.1) and describe the components and inputs of our learned optimizer (Section 4.2). To ensure long-horizon stability, we employ two complementary strategies. The first, described in Section 4.1, identifies potential sources of instability and incorporates losses to mitigate them. The second strategy adopts a data-centric approach, allowing the optimizer to encounter a variety of intermediate states along actual optimization trajectories, and is described in Section 4.3. Model architecture and hyper-parameters are detailed in the sup. mat.

4.1 Meta Training

A learned optimizer is meta-trained across a collection of 3D scenes $\{\mathcal{V}^j\}_{j=1}^{V}$, where each scene $\mathcal{V}^j$ consists of a set of context views used during optimization and a fixed set of target views used for evaluation. For simplicity, we omit the index j as all quantities are per scene. Fig. 3 illustrates the training procedure.

Inner loop. At each inner step t, the current Gaussians are rendered for a batch of context views, and the inner loss $\mathcal{L}_{\text{inner}}(\mathbf{I}, \tilde{\mathbf{I}}(\boldsymbol{\mathcal{G}}_t))$ is computed. The resulting gradients wrt. the Gaussian parameters $\nabla_{\boldsymbol{\mathcal{G}}_t}$ are passed as input to the optimizer, which predicts parameter updates $\Delta_{\boldsymbol{\mathcal{G}}_t}$. These updates are applied to obtain $\boldsymbol{\mathcal{G}}_{t+1}$, the next set of Gaussians for the following inner iteration. After τ inner iterations, where τ is sampled uniformly from [1,6], the scene reaches the updated state $\boldsymbol{\mathcal{G}}_{t+\tau}(\boldsymbol{\theta}_{t_{\text{meta}}})$.

Meta loop. Throughout the τ inner iterations, both context and target views are rendered at each step to supervise the meta-optimizer. The meta-loss

$$\mathcal{L}_{\text{meta}}(\mathbf{I}, \tilde{\mathbf{I}}(\boldsymbol{\mathcal{G}}_{t+\tau}(\boldsymbol{\theta}_{t_{\text{meta}}}))) \tag{6}$$

is then computed using these renderings to evaluate the effectiveness of the predicted updates along the optimization trajectory. This induces the meta-optimizer to produce updates that generalize to novel views, rather than overfitting to the context view set. The meta loss gradients wrt. the optimizer parameters, $\nabla_{\boldsymbol{\theta}_{t_{\text{meta}}}} = \nabla_{\boldsymbol{\theta}_{t_{\text{meta}}}} \mathcal{L}_{\text{meta}}$, are used to update $\boldsymbol{\theta}_{t_{\text{meta}}}$ using a general-purpose optimizer (Adam [22]).

Losses. For the inner loss, we adopt the standard 3DGS formulation:

$$\mathcal{L}_{\text{inner}} = 0.8\,\ell_1(\mathbf{I}, \tilde{\mathbf{I}}) + 0.2\,\text{D-SSIM}(\mathbf{I}, \tilde{\mathbf{I}}) \tag{7}$$

For the meta loss, we combine three components: (1) a rendering loss ($\mathcal{L}_{\text{render}}$) that supervises reconstruction quality, (2) a low-visibility supervision term ($\mathcal{L}_{\text{lvs}}$) that regularizes weakly supervised or unsupervised Gaussians, and (3) a stability term ($\mathcal{L}_{\text{stab}}$) that encourages monotonic improvement:

$$\mathcal{L}_{\text{meta}} = \mathcal{L}_{\text{render}} + \mathcal{L}_{\text{lvs}} + \mathcal{L}_{\text{stab}} \tag{8}$$

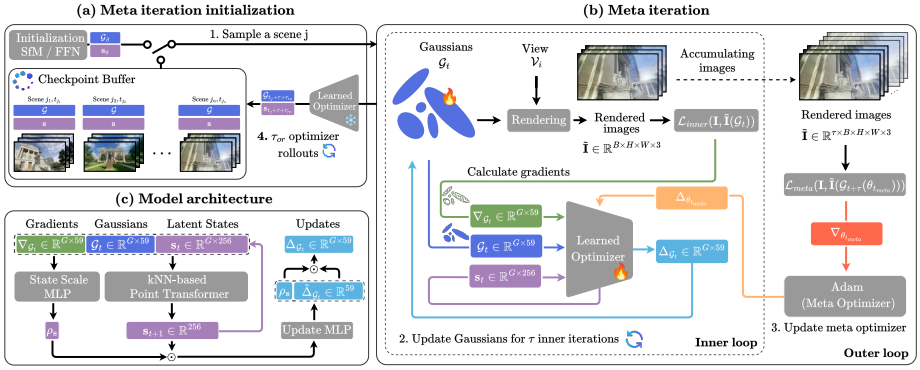


Fig. 3: Learn2Splat Meta-training and Architecture. (a) Meta iteration initialization. During meta-training, we iterate over different 3D scenes. At each meta-iteration, a scene is sampled and its Gaussians are initialized using either (1) SfM or FFN points at $t = 0$, or (2) an intermediate state drawn from the *Checkpoint Buffer*. At the end of each meta iteration, the updated scene is randomly pushed back into the buffer, after applying additional rollout steps using a frozen version of the learned optimizer (Sec. 4.3). **(b) Meta iteration.** Starting from the scene sampled in (a), the *inner loop* (dashed block) rolls out the learned optimizer for τ iterations, predicting Gaussian parameter updates that iteratively refine the scene representation. Once the inner loop completes, the meta iteration (outer block) evaluates the reconstruction performance and backpropagates the resulting meta-gradients to update the optimizer's parameters. By observing a different scene at each meta-iteration, the optimizer learns update rules that generalize across scenes. **(c) Model architecture.** Our model comprises two parallel branches: a *State Scale MLP*, which predicts state-scaling coefficients from Adam-normalized gradients, and a *kNN-based Point Transformer*, which predicts updated per-Gaussian latent states (Sec. 4.2). The scaled latent states are fed into the *Update MLP*, which predicts the final Gaussian parameter updates (Sec. 4.2). $\odot$ denotes element-wise multiplication, dashed lines indicate concatenation.

The rendering loss is defined following ReSplat [47], and is computed as an exponentially weighted sum over τ inner steps

$$\mathcal{L}_{\text{render}} = \sum_{t=0}^{\tau-1} \gamma^{\tau-1-t} \Big[\ell_1(\mathbf{I}_t, \tilde{\mathbf{I}}_t) + 0.5\, \text{LPIPS}(\mathbf{I}_t, \tilde{\mathbf{I}}_t) \Big] \tag{9}$$

where $\gamma = 0.9$. Although this loss is effective, it provides limited supervision for Gaussians with negligible contributions to the rendered images. Due to their weak influence on the loss, these primitives do not receive meaningful feedback, allowing the optimizer to produce unconstrained updates. While such updates may be harmless in the short term, they accumulate over longer optimization horizons, ultimately degrading rendering quality. To address this, we introduce a low-visibility supervision loss ($\mathcal{L}_{\text{lvs}}$) that penalizes updates for weakly supervised Gaussians. Specifically, we add an ℓ_1 loss on the predicted updates whenever the gradient magnitude falls below a small threshold ($\varepsilon = 10^{-8}$). We additionally apply this loss to updates whose sign differs from that of the Adam gradient (more

details in sup. mat.). Additionally, we introduce a *stability* loss that encourages the optimizer to produce monotonically improving reconstructions. This loss is only computed on target views, as they remain constant throughout a meta-iteration. Specifically, we penalize inner iterations where the ℓ_1 error increases relative to the previous step (sg$[\cdot]$ denotes the stop-gradient operation):

$$\mathcal{L}_{\text{stab}} = \sum_{t=1}^{\tau-1} \max\left(0, \ell_1(\mathbf{I}_t, \tilde{\mathbf{I}}_t) - \text{sg}[\ell_1(\mathbf{I}_{t-1}, \tilde{\mathbf{I}}_{t-1})]\right) \tag{10}$$

4.2 Model Overview

Our learned optimizer operates on Gaussian primitives, maintaining an internal per-primitive state and updating the Gaussian parameters at every iteration. An overview of this pipeline is shown in Fig. 3, with further details on the model architecture available in the supplementary material.

Model Input. We build upon ReSplat [47], which refines pixel-aligned Gaussian parameters through iterative updates driven by per-pixel feature-space errors. While effective, this limits flexibility across different initializations and ignores inter-pixel and multi-view dependencies. To address these issues, we replace the error signal with image-loss gradients computed with respect to the Gaussian parameters. However, directly using gradients is non-trivial: their magnitudes can vary by several orders, and often reach extremely small values (e.g., 10^{-8}). While such gradients remain informative for a non-learned optimizer, they lie outside the typical numerical range that neural networks handle effectively. Prior methods [14,29], normalize each gradient entry by the maximum absolute value of that parameter within the current scene. While this normalization scheme can stabilize training, it induces a counterintuitive effect compared to standard optimization: as training progresses and the maximum values decrease, the effective gradient magnitudes grow. Inspired by learned optimizers [43], we instead feed the network Adam-style (moment-averaged and normalized) gradients. These smoothed gradients provide natural per-parameter normalization and encode optimization history through moment averaging. At iteration t, the model process the full batch of Gaussians $\boldsymbol{\mathcal{G}}_t$ jointly, taking as input the per-Gaussian gradients $\nabla_{\boldsymbol{\mathcal{G}}_t} \in \mathbb{R}^{G\times 59}$, the current Gaussian parameters $\boldsymbol{\mathcal{G}}_t \in \mathbb{R}^{G\times 59}$, and the latent Gaussian states $\mathbf{s}_t \in \mathbb{R}^{G\times 256}$. These are concatenated along the feature dimension to form a unified representation $\mathbf{x} = [\nabla_{\boldsymbol{\mathcal{G}}_t}, \boldsymbol{\mathcal{G}}_t, \mathbf{s}_t] \in \mathbb{R}^{G\times(59+59+256)}$.

Latent State Predictions. The optimizer consists of two parallel branches operating on the unified representation $\mathbf{x}$. The first branch is a kNN-based *Point Transformer* [44,45,51], which applies self-attention to each Gaussian by attending to its k nearest neighbor (kNN) in 3D space. The output is then the updated latent states $\mathbf{s}_{t+1} \in \mathbb{R}^{G\times 256}$, encoding per-primitive contextual and temporal information. However, using the standard normalization layers within the transformer suppresses input gradient scale information, crucial for ensuring that

predicted updates diminish as the loss decreases. To restore this information, the *State Scale MLP* branch predicts per-Gaussian scaling coefficients $\boldsymbol{\rho}_{\mathbf{s}} \in \mathbb{R}^G$ (non-negative), which modulate the magnitude of the state updates. The resulting scaled states are computed as: $\tilde{\mathbf{s}}_{t+1} = \boldsymbol{\rho}_{\mathbf{s}} \odot \mathbf{s}_{t+1}$, where $\odot$ denotes element-wise multiplication applied per Gaussian, i.e., each Gaussian's state vector in $\mathbf{s}_{t+1}$ is scaled by its corresponding scalar in $\boldsymbol{\rho}_{\mathbf{s}}$. The unscaled states $\mathbf{s}_{t+1}$ are preserved for the next optimization step, while the scaled states $\tilde{\mathbf{s}}_{t+1}$ are forwarded to the parameter update module. The latent states $\mathbf{s}_0$ can be initialized by an FFN or sampled from a standard normal distribution (see Sec. 5).

Updates Predictions. To obtain the actual parameter updates, we employ an *Update MLP* that maps the scaled states $\tilde{\mathbf{s}}_{t+1}$ to a set of per-Gaussian parameter updates $\mathbf{O}_{\boldsymbol{\mathcal{G}}_t} \in \mathbb{R}^{G \times 60}$. Its output is split into two parts per Gaussian: a 59-dimensional unit-length vector $\tilde{\Delta}_{\boldsymbol{\mathcal{G}}_t}$, normalized to represent the update direction, and a single non-negative scalar $\boldsymbol{\rho}_{\Delta_t}$, controlling the update magnitude. The final parameter updates are computed as $\Delta_{\boldsymbol{\mathcal{G}}_t} = \boldsymbol{\rho}_{\Delta_t} \odot \tilde{\Delta}_{\boldsymbol{\mathcal{G}}_t}$, with independent control over the direction and magnitude of each update. Finally, the Gaussians of the next iteration $t+1$ are computed based on (4), as $\boldsymbol{\mathcal{G}}_{t+1} = \boldsymbol{\mathcal{G}}_t - \Delta_{\boldsymbol{\mathcal{G}}_t}$.

4.3 Long Horizon Training

A key design principle of our learned optimizer is *long-horizon stability*, requiring that predicted parameter updates diminish as the loss gradients diminish. This prevents quality degradation over extended optimization horizons and allows the optimizer to be applied beyond its training distribution, too. We aim for this behavior to emerge as an intrinsic property of the learned optimizer, rather than being enforced through external scheduling mechanisms such as time encoding or LR schedules tied to a predefined number of iterations.

Checkpoint Buffer. Learning long-horizon 3DGS reconstruction requires exposing the optimizer to diverse states, from large early gradients to fine late-stage refinements. However, naively extending the inner loop is computationally prohibitive and violates the i.i.d. assumption, as the optimizer would repeatedly encounter large gradients early and small ones later, hindering stable and generalizable learning. To address this, we introduce a *checkpoint buffer* that stores intermediate scene states from previous meta-iterations (See Fig. 3(a)). At each meta-iteration, a new scene is sampled with probability $1 - p_{\text{buffer}}$, or an existing checkpoint is resampled with probability p_{buffer}, allowing the optimizer to resume from diverse points along the optimization trajectory without extending the inner loop. Then the optimizer is unrolled for a small number of inner steps. Finally, the updated state is pushed back into the buffer with a probability of p_{push} for newly initialized scenes and $p_{\text{push-back}}$ for resampled ones. Each stored checkpoint contains the Gaussian parameters and relevant optimizer states, including Adam moments and per-Gaussian latent vectors, enabling seamless continuation of optimization across meta-iterations. As a result, the optimizer is exposed to

a balanced distribution of optimization states, enabling it to develop update behaviors that remain effective throughout the full optimization trajectory, from rapid early progress to fine-grained late-stage refinements.

Optimizer Rollout. Inspired by policy rollout in reinforcement learning [8], we introduce an *optimizer rollout* strategy to further extend observed optimization horizons. Before storing a scene in the buffer, we further optimize its parameters using the currently learned optimizer, while keeping the model frozen. This promotes Gaussians along trajectories resembling those encountered during inference, helping the learned optimizer recover from its own mistakes. The number of rollout iterations is sampled at random in $[1, \tau_a]$, where τ_a is linearly increased from 1 to 50 during the first $10,000$ meta training iterations, effectively implementing easy-to-hard curriculum learning.

5 Experiments

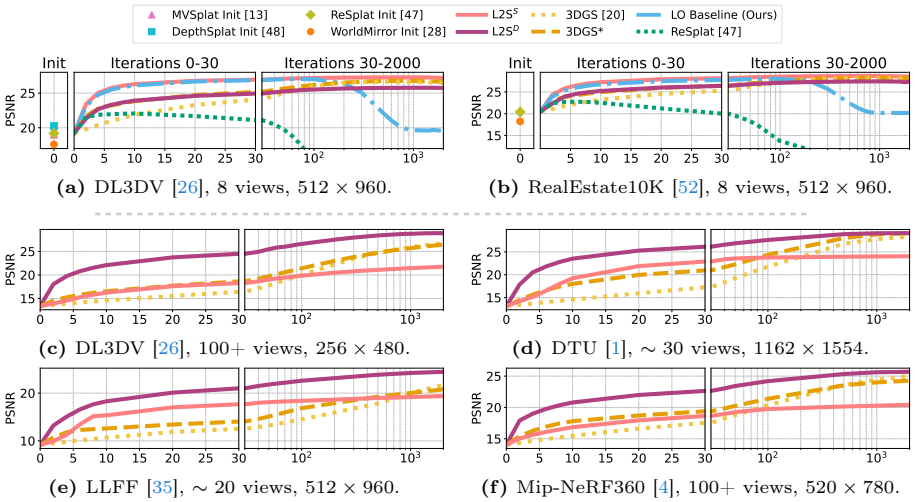
We first detail our training setup (Sec. 5.1) and then present our results (Sec. 5.2).

5.1 Training Details

Learn2Splat can be applied in both sparse and dense settings. We demonstrate this by training under two distinct configurations of the DL3DV dataset [26], which contains 9,896 scenes. First, we train in a *sparse-view*, *forward-facing* setup using the initialization from ReSplat [47] (L2S$^{\mathbf{S}}$). Second, we train in a *dense-view*, *large-baseline* setup using SfM-initialized Gaussians and randomly sampled latent states (L2S$^{\mathbf{D}}$), while applying data augmentation by randomly sampling 10–100% of the initial points. We initialize with SfM points since they are a free by-product of camera estimation, commonly used in 3DGS pipelines, and provide a sparse starting point that highlights our optimizer's ability to recover from poor initializations. During training, L2S$^{\mathbf{S}}$ uses the same 8 context views across all inner steps, whereas L2S$^{\mathbf{D}}$ samples 8 views per iteration from all viewpoints via furthest point sampling to maximize coverage. Both settings use low-resolution images (256×448) and 8 context views to reduce computational cost; 6 target views are sampled per optimization trajectory and kept fixed during inner optimization. At each inner iteration, Gaussian parameters and gradients are detached before being fed to the network, while the latent state remains differentiable, allowing gradients to flow between iterations only through the states. Our framework is implemented on `gsplat` [49]. The learned optimizer is trained end-to-end in PyTorch with mixed precision for 50k meta-iterations on 4 NVIDIA A100 GPUs using Adam as the meta-optimizer (LR 10^{-4}).

5.2 Results

Direct comparison with prior learned optimizers is not feasible, as their code is unavailable (G3R) or their models are trained for geometry reconstruction



(a) DL3DV [26], 8 views, 512 × 960. **(b)** RealEstate10K [52], 8 views, 512 × 960.

(c) DL3DV [26], 100+ views, 256 × 480. **(d)** DTU [1], ∼ 30 views, 1162 × 1554.

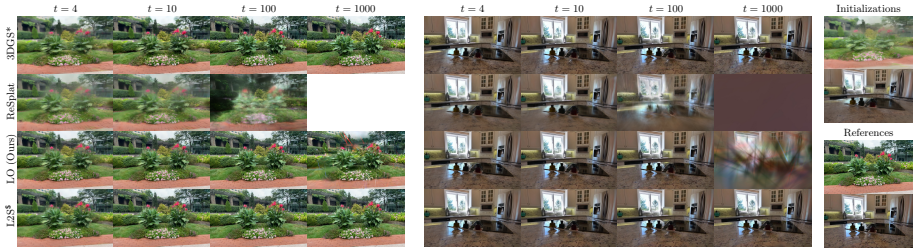
(e) LLFF [35], ∼ 20 views, 512 × 960. **(f)** Mip-NeRF360 [4], 100+ views, 520 × 780.

Fig. 4: Quantitative Evaluation. In each setting, all iterative methods share the same initialization and views configuration. (**a-b**) **Sparse**: All methods initialized with ReSplat and use the same 8 views in every iteration. Here, the *Init* column represents feed-forward baselines. (**c-f**) **Dense setting**: All methods initialized with SfM points, sampling 8 views from the available views at each iteration. All iterative methods are optimized for 2000 iterations, and PSNR is reported for evaluation.

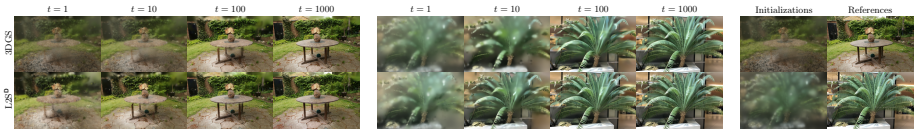
rather than novel view synthesis (QuickSplat). Therefore, we implement our own Learned Optimizer (LO) baseline, which shares the ReSplat model architecture (including Adam-style gradients) but incorporates time encoding conditioning for update prediction and a LR schedule following G3R. It does not include our low-visibility and stability losses and the two scaling factors applied to the state vector and predicted updates. LO is trained with the original G3R meta-learning scheme on the same data and using the same initialization as L2S$^{\mathbf{S}}$.

We evaluate L2S$^{\mathbf{S}}$ and L2S$^{\mathbf{D}}$ in both *sparse-view*, *forward-facing* and *dense-view*, *large-baseline* settings. For the former, baselines include ReSplat, our LO baseline, 3DGS (original implementation and Adam hyper-parameters suggested by the authors) and 3DGS* (result of a grid search over Adam hyper-parameters on a subset of DL3DV test scenes ($5\times$ LR, $\beta_1 = 0.99$, $\beta_2 = 0.999$). For the latter, baselines are 3DGS and 3DGS*. Quantitative and qualitative results are presented in Fig. 4 and Fig. 5, respectively. *No setting uses densification or pruning*, as these heuristics are orthogonal to our goal of comparing optimizers under equal scene capacity. For efficiency, k-NN is computed every 100 iterations at test time. Detailed qualitative results can be found in the sup. mat.

Sparse Setting. We evaluate L2S$^{\mathbf{S}}$ and L2S$^{\mathbf{D}}$ in the sparse, forward-facing setting to assess zero-shot generalization across datasets and resolutions, with initialization and views selection matching L2S$^{\mathbf{S}}$ training setup. All scenes are optimized for 2000 iterations. Experiments are conducted on high-resolution scenes from DL3DV [26] (Fig. 4(a)) and RealEstate10K [52] (Fig. 4(b)). Note that the ReSplat's initialization produces 57K primitives at low resolution (during train-



(a) Two scenes from DL3DV [26] and RealEstate10K [52] in the sparse-views setting.



(b) Two scenes from Mip-NeRF360 [4] and LLFF [35], in the dense-views setting.

Fig. 5: Qualitative Results. (**a**) Sparse setting results with ReSplat initialization, using the same 8 views in every iteration. (**b**) Dense setting results with SfM initialization, sampling 8 views per iteration from all available views. Both L2S$^{\mathbf{S}}$ and L2S$^{\mathbf{D}}$ demonstrate zero-shot generalization to higher resolutions and different datasets.

ing) and 245K at high resolution (testing configuration). Our results (L2S$^{\mathbf{S}}$, L2S$^{\mathbf{D}}$) demonstrate accelerated early PSNR gains while maintaining the stability required for long-horizon optimization. Notably, we achieve higher PSNR in fewer iterations than both the original 3DGS and ReSplat. Our LO baseline initially reaches comparable performance in both settings, but collapses when optimization continues. L2S$^{\mathbf{D}}$ performs worse than L2S$^{\mathbf{S}}$, as ReSplat initialization produces a denser Gaussian distribution than L2S$^{\mathbf{D}}$ was trained with. Moreover, L2S$^{\mathbf{S}}$ utilizes feature vectors from the initialization to construct the latent vectors. Nevertheless, L2S$^{\mathbf{D}}$ it performs roughly on par with 3DGS.

Dense Setting. We further evaluate L2S$^{\mathbf{S}}$ and L2S$^{\mathbf{D}}$ on dense-view scenes to assess zero-shot generalization across varying view counts and resolutions. All scenes are initialized from sparse SfM point clouds and are optimized for 2000 iterations. At each iteration, we sample mini-batches of 8 views, matching the dense-training configuration. Experiments are conducted on scenes from DL3DV [26] (low-resolution, Fig. 4(c)), DTU [1] (Fig. 4(d)), LLFF [35] (Fig. 4(e)), and Mip-NeRF360 [4] (Fig. 4(f)) datasets. In this regime, the model trained for this setting, L2S$^{\mathbf{D}}$, outperforms 3DGS in early iterations and reaches better PSNR at convergence. L2S$^{\mathbf{S}}$ matches or exceeds 3DGS early on but saturates later.

Beyond scene differences, we hypothesize that L2S$^{\mathbf{S}}$ learns to exploit the fixed set of views used during inner iterations, potentially encoding view-dependent information in the per-Gaussian latent states. While beneficial in the sparse-view regime, this dependency harms performance in the dense-view setting where views are randomly sampled. Conversely, L2S$^{\mathbf{D}}$ is exposed to new views at each iteration during meta-training, preventing it from learning such dependencies. This may also explain its weaker performance in the sparse-view regime. Addi-

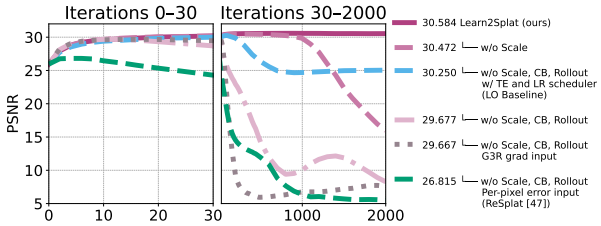


Fig. 6: Ablation Study. We ablate our design choices discussed in Section 4.3 on L2S$^{\mathbf{S}}$ training. Results are commented in Sec. 5.2.

tionally, we highlight Adam's sensitivity to the learning rate: settings that work best in the sparse case do not transfer to the dense case.

Ablation Study. We show ablations of our contributions in Fig. 6, validating our design decisions. Starting from vanilla ReSplat [47] (green), long-horizon stability is progressively increased by replacing the per-pixel error inputs with gradients, first using the G3R normalization [14] (brown), then Adam-style normalization (pink), which further slows degradation. Note that adding the LR scheduler and time encoding (blue), as used in prior work [14,29], does not prevent degradation. Finally, progressively incorporating our meta-training scheme—checkpoint buffer (CB), optimizer rollouts, and predicted scaling factors—yields our final model (purple), which remains stable and avoids degradation even when evaluated for 15× longer horizons than seen during training.

Runtimes. We evaluated the overhead of our optimizer compared to Adam. Iterations are 2–2.5× slower on average. However, our updates yield better reconstruction quality in fewer iterations, particularly during early stages (Fig. 4). We provide full runtimes evaluation in the sup. mat. Note that our implementation is unoptimized research code; runtimes could be reduced with a more engineered implementation.

6 Conclusions

We introduced Learn2Splat, a learned optimizer for 3DGS that reaches higher reconstruction quality with fewer iterations in early stages, while remaining effective across long optimization horizons. Its effectiveness stems from architecture, losses, and a meta-learning scheme. Empirically, Learn2Splat performs best in its training domain (sparse or dense views) and generalizes zero-shot to higher resolutions and new datasets. This points toward domain-specialized optimizers for efficient, robust 3DGS reconstruction.

Future Work. In complex scenes, our optimizer can saturate early, likely due to overly conservative updates. Future work will address this by making the learned optimizer more explicitly view-aware and by introducing per-parameter-group adaptive scaling instead of a global scaling factor. We also plan to develop a unified optimizer that handles both sparse and dense view regimes more efficiently, while incorporating learnable densification and pruning mechanisms.

Acknowledgements. Andreas Geiger was supported by the ERC Starting Grant LEGO-3D (850533) and the DFG EXC number 2064/1 - project number 390727645. Gerard Pons-Moll and Andreas Geiger are members of the Machine Learning Cluster of Excellence, EXC number 2064/1 - Project number 390727645. Gerard Pons-moll is endowed by the Carl Zeiss Foundation. Stefano Esposito acknowledges travel support from the European Union's Horizon 2020 research and innovation program under ELISE Grant Agreement No. 951847. We thank the International Max Planck Research School for Intelligent Systems (IMPRS-IS) for supporting Patricia Gschoßmann and Amit Peleg. We acknowledge support from the Deutsche Forschungsgemeinschaft (DFG, German Research Foundation) under Germany's Excellence Strategy (EXC number 2064/1, project number 390727645).

References

1. Aanæs, H., Jensen, R.R., Vogiatzis, G., Tola, E., Dahl, A.B.: Large-scale data for multiple-view stereopsis. International Journal of Computer Vision (IJCV) (2016) 3, 12, 13, 21, 35, 40
2. Agarwal, S., Snavely, N., Simon, I., Seitz, S.M., Szeliski, R.: Building rome in a day. In: Proc. of the IEEE International Conf. on Computer Vision (ICCV) (2009) 3, 21
3. Andrychowicz, M., Denil, M., Gomez, S., Hoffman, M.W., Pfau, D., Schaul, T., Shillingford, B., De Freitas, N.: Learning to learn by gradient descent by gradient descent. Advances in Neural Information Processing Systems (NeurIPS) (2016) 2, 4
4. Barron, J.T., Mildenhall, B., Verbin, D., Srinivasan, P.P., Hedman, P.: Mip-nerf 360: Unbounded anti-aliased neural radiance fields. Proc. IEEE Conf. on Computer Vision and Pattern Recognition (CVPR) (2022) 3, 12, 13, 21, 35, 40
5. Bello, I., Zoph, B., Vasudevan, V., Le, Q.V.: Neural optimizer search with reinforcement learning. In: Proc. of the International Conf. on Machine learning (ICML) (2017) 2
6. Bengio, S., Bengio, Y., Cloutier, J., Gecsei, J.: On the optimization of a synaptic learning rule. In: Optimality in Biological and Artificial Networks (1992) 4
7. Bengio, Y., Bengio, S., Cloutier, J.: Learning a synaptic learning rule. Citeseer (1990) 4
8. Bertsekas, D.: Multiagent reinforcement learning: Rollout and policy iteration. IEEE/CAA Journal of Automatica Sinica (2021) 11
9. Bulò, S.R., Porzi, L., Kontschieder, P.: Revising densification in gaussian splatting. In: Proc. of the European Conf. on Computer Vision (ECCV) (2024) 4
10. Charatan, D., Li, S., Tagliasacchi, A., Sitzmann, V.: pixelsplat: 3d gaussian splats from image pairs for scalable generalizable 3d reconstruction. In: Proc. IEEE Conf. on Computer Vision and Pattern Recognition (CVPR) (2024) 2, 4
11. Chen, T., Chen, X., Chen, W., Heaton, H., Liu, J., Wang, Z., Yin, W.: Learning to optimize: A primer and a benchmark. Journal of Machine Learning Research (JMLR) (2022) 4
12. Chen, T., Xiang, W., Han, K., Lu, Y., Wu, D., Liu, G., Kompella, R.R.: Gifsplat: Generative prior-guided iterative feed-forward 3d gaussian splatting from sparse views. arXiv:2602.22571 (2026) 5

13. Chen, Y., Xu, H., Zheng, C., Zhuang, B., Pollefeys, M., Geiger, A., Cham, T.J., Cai, J.: Mvsplat: Efficient 3d gaussian splatting from sparse multi-view images. In: Proc. of the European Conf. on Computer Vision (ECCV) (2024) 2, 4, 34
14. Chen, Y., Wang, J., Yang, Z., Manivasagam, S., Urtasun, R.: G3r: Gradient guided generalizable reconstruction. In: Proc. of the European Conf. on Computer Vision (ECCV) (2024) 1, 3, 4, 5, 9, 14, 28, 30
15. Corona, E., Pons-Moll, G., Alenyà, G., Moreno-Noguer, F.: Learned vertex descent: A new direction for 3d human model fitting. In: Proc. of the European Conf. on Computer Vision (ECCV) (2022) 4
16. Deng, Y., Han, L., Lin, T., Li, L., Zhang, J., Fang, L.: Efflife: Efficient light field generation via hierarchical sparse gradient descent. arXiv:2307.03017 (2023) 4
17. Flynn, J., Broxton, M., Debevec, P.E., DuVall, M., Fyffe, G., Overbeck, R.S., Snavely, N., Tucker, R.: Deepview: View synthesis with learned gradient descent. In: Proc. IEEE Conf. on Computer Vision and Pattern Recognition (CVPR) (2019) 4
18. Höllein, L., Božič, A., Zollhöfer, M., Nießner, M.: 3dgs-lm: Faster gaussian-splatting optimization with levenberg-marquardt. In: Proc. of the IEEE International Conf. on Computer Vision (ICCV) (2025) 4
19. Jiang, L., Mao, Y., Xu, L., Lu, T., Ren, K., Jin, Y., Xu, X., Yu, M., Pang, J., Zhao, F., et al.: Anysplat: Feed-forward 3d gaussian splatting from unconstrained views. ACM Trans. on Graphics (2025) 2, 4
20. Kerbl, B., Kopanas, G., Leimkühler, T., Drettakis, G.: 3dgs: 3d gaussian splatting for real-time radiance field rendering. ACM Trans. on Graphics (2023) 1, 2, 4, 6, 19, 21, 27, 30, 33, 34, 37, 38, 40
21. Kiefer, J., Wolfowitz, J.: Stochastic estimation of the maximum of a regression function. The annals of Mathematical Statistics (1952) 2
22. Kingma, D.P., Ba, J.: Adam: A method for stochastic optimization. In: Proc. of the International Conf. on Learning Representations (ICLR) (2015) 2, 4, 7
23. Kingma, D.P., Ba, J.: Adam: A method for stochastic optimization. In: Bengio, Y., LeCun, Y. (eds.) Proc. of the International Conf. on Learning Representations (ICLR) (2015) 19
24. Kotovenko, D., Grebenkova, O., Ommer, B.: Edgs: Eliminating densification for efficient convergence of 3dgs. arXiv:2504.13204 (2025) 4
25. Lan, L., Shao, T., Lu, Z., Zhang, Y., Jiang, C., Yang, Y.: 3dgs2: Near second-order converging 3d gaussian splatting. In: Proceedings of the Special Interest Group on Computer Graphics and Interactive Techniques Conference Conference Papers (2025) 4
26. Ling, L., Sheng, Y., Tu, Z., Zhao, W., Xin, C., Wan, K., Yu, L., Guo, Q., Yu, Z., Lu, Y., et al.: Dl3dv-10k: A large-scale scene dataset for deep learning-based 3d vision. In: Proc. IEEE Conf. on Computer Vision and Pattern Recognition (CVPR) (2024) 1, 11, 12, 13, 21, 22, 34, 35, 38, 39, 40
27. Liu, T., Wang, G., Hu, S., Shen, L., Ye, X., Zang, Y., Cao, Z., Li, W., Liu, Z.: Mvsgaussian: Fast generalizable gaussian splatting reconstruction from multi-view stereo. In: Proc. of the European Conf. on Computer Vision (ECCV) (2024) 2, 4
28. Liu, Y., Min, Z., Wang, Z., Wu, J., Wang, T., Yuan, Y., Luo, Y., Guo, C.: Worldmirror: Universal 3d world reconstruction with any-prior prompting. arXiv:2510.10726 (2025) 2, 4, 34
29. Liu, Y.C., Höllein, L., Nießner, M., Dai, A.: Quicksplat: Fast 3d surface reconstruction via learned gaussian initialization. In: Proc. of the IEEE International Conf. on Computer Vision (ICCV) (2025) 1, 3, 4, 5, 9, 14, 28

30. Lu, T., Yu, M., Xu, L., Xiangli, Y., Wang, L., Lin, D., Dai, B.: Scaffold-gs: Structured 3d gaussians for view-adaptive rendering. In: Proc. IEEE Conf. on Computer Vision and Pattern Recognition (CVPR) (2024) 4
31. Lv, Z., Dellaert, F., Rehg, J.M., Geiger, A.: Taking a deeper look at the inverse compositional algorithm. In: Proc. IEEE Conf. on Computer Vision and Pattern Recognition (CVPR) (2019) 4
32. Mallick, S.S., Goel, R., Kerbl, B., Steinberger, M., Carrasco, F.V., De La Torre, F.: Taming 3dgs: High-quality radiance fields with limited resources. ACM Trans. on Graphics (2024) 4
33. Metz, L., Harrison, J., Freeman, C.D., Merchant, A., Beyer, L., Bradbury, J., Agrawal, N., Poole, B., Mordatch, I., Roberts, A., et al.: Velo: Training versatile learned optimizers by scaling up. arXiv:2211.09760 (2022) 4
34. Metz, L., Maheswaranathan, N., Freeman, C.D., Poole, B., Sohl-Dickstein, J.: Tasks, stability, architecture, and compute: Training more effective learned optimizers, and using them to train themselves. arXiv:2009.11243 (2020) 4
35. Mildenhall, B., Srinivasan, P.P., Ortiz-Cayon, R., Kalantari, N.K., Ramamoorthi, R., Ng, R., Kar, A.: Local light field fusion: Practical view synthesis with prescriptive sampling guidelines. ACM Trans. on Graphics (2019) 3, 12, 13, 21, 35, 37, 40
36. MildenhallandBen, P, S., TancikandMatthew, T, B., RamamoorthiandRavi, NgandRen: NeRF: Representing scenes as neural radiance fields for view synthesis. In: Proc. of the European Conf. on Computer Vision (ECCV) (2020) 28
37. Nichol, A.Q., Dhariwal, P.: Improved denoising diffusion probabilistic models. In: Proc. of the International Conf. on Machine learning (ICML) (2021) 28
38. Robbins, H., Monro, S.: A stochastic approximation method. The annals of Mathematical Statistics (1951) 2, 4
39. Szymanowicz, S., Rupprecht, C., Vedaldi, A.: Splatter image: Ultra-fast single-view 3d reconstruction. In: Proc. IEEE Conf. on Computer Vision and Pattern Recognition (CVPR) (2024) 4
40. Vaswani, A., Shazeer, N., Parmar, N., Uszkoreit, J., Jones, L., Gomez, A.N., Kaiser, L., Polosukhin, I.: Attention is all you need. In: Advances in Neural Information Processing Systems (NeurIPS) (2017) 28
41. Wang, W., Chen, D.Y., Zhang, Z., Shi, D., Liu, A., Zhuang, B.: Zpressor: Bottleneck-aware compression for scalable feed-forward 3dgs. arXiv:2505.23734 (2025) 4
42. Wang, W., Chen, Y., Zhang, Z., Liu, H., Wang, H., Feng, Z., Qin, W., Zhu, Z., Chen, D.Y., Zhuang, B.: Volsplat: Rethinking feed-forward 3d gaussian splatting with voxel-aligned prediction. arXiv:2509.19297 (2025) 4
43. Wichrowska, O., Maheswaranathan, N., Hoffman, M.W., Colmenarejo, S.G., Denil, M., de Freitas, N., Sohl-Dickstein, J.: Learned optimizers that scale and generalize. In: Proc. of the International Conf. on Machine learning (ICML) (2017) 2, 4, 9
44. Wu, X., Jiang, L., Wang, P.S., Liu, Z., Liu, X., Qiao, Y., Ouyang, W., He, T., Zhao, H.: Point transformer v3: Simpler faster stronger. In: Proc. IEEE Conf. on Computer Vision and Pattern Recognition (CVPR) (2024) 9
45. Wu, X., Lao, Y., Jiang, L., Liu, X., Zhao, H.: Point transformer v2: Grouped vector attention and partition-based pooling. Advances in Neural Information Processing Systems (NeurIPS) (2022) 9
46. Xiong, X., De la Torre, F.: Supervised descent method and its applications to face alignment. In: Proc. IEEE Conf. on Computer Vision and Pattern Recognition (CVPR) (2013) 4

47. Xu, H., Barath, D., Geiger, A., Pollefeys, M.: Resplat: Learning recurrent gaussian splatting. arXiv:2510.08575 (2025) 1, 2, 3, 4, 5, 8, 9, 11, 14, 20, 21, 23, 28, 30, 34, 36
48. Xu, H., Peng, S., Wang, F., Blum, H., Barath, D., Geiger, A., Pollefeys, M.: Depthsplat: Connecting gaussian splatting and depth. In: Proc. IEEE Conf. on Computer Vision and Pattern Recognition (CVPR) (2025) 2, 4, 34
49. Ye, V., Li, R., Kerr, J., Turkulainen, M., Yi, B., Pan, Z., Seiskari, O., Ye, J., Hu, J., Tancik, M., Kanazawa, A.: gsplat: An open-source library for gaussian splatting. Journal of Machine Learning Research (JMLR) (2025) 11
50. Zhang, J., Zhan, F., Shao, L., Lu, S.: Sogs: Second-order anchor for advanced 3d gaussian splatting. In: Proc. IEEE Conf. on Computer Vision and Pattern Recognition (CVPR) (2025) 4
51. Zhao, H., Jiang, L., Jia, J., Torr, P.H., Koltun, V.: Point transformer. In: Proc. of the IEEE International Conf. on Computer Vision (ICCV) (2021) 9
52. Zhou, T., Tucker, R., Flynn, J., Fyffe, G., Snavely, N.: Stereo magnification: learning view synthesis using multiplane images. ACM Trans. on Graphics (2018) 3, 12, 13, 21, 34, 36, 39

Supplementary Material

We provide additional technical details and results complementing the main paper. Tab. 4 summarizes the mathematical notation used throughout the paper. We first review the Adam [23] update rule (Section A.1) and derive the 3DGS rendering formulation (Section A.2). Section B discusses scene initialization strategies, Section C introduces the datasets used in our experiments. Section D details the meta-training procedure, including the checkpoint buffer, optimizer rollout strategy, low-visibility loss, stability loss, and additional training details (Section D.1). Further architectural details are given in Section E, while Section F describes the baselines and their implementations. Section G presents additional qualitative and quantitative results. Finally, Section H analyzes the optimization dynamics of our optimizer compared to Adam.

A Preliminaries

For completeness, we provide the full Adam [23] algorithm in Sec. A.1 and the full 3DGS [20] rendering derivation in Sec. A.2.

A.1 Adam

The general update rule (Eq. (3)) can be written as follows,

$$\begin{aligned} \mathbf{m}_t &= \beta_1 \mathbf{m}_{t-1} + (1-\beta_1)\nabla_{\boldsymbol{\mathcal{G}}_t} \\ \mathbf{v}_t &= \beta_2 \mathbf{v}_{t-1} + (1-\beta_2)\left(\nabla_{\boldsymbol{\mathcal{G}}_t}\right)^2 \\ \hat{\mathbf{m}}_t &= \frac{\mathbf{m}_t}{1-\beta_1^t}, \quad \hat{\mathbf{v}}_t = \frac{\mathbf{v}_t}{1-\beta_2^t} \\ f_{\text{Adam}}\left(\nabla_{\boldsymbol{\mathcal{G}}_t}\right) &= \frac{\eta_t}{\sqrt{\hat{\mathbf{v}}_t}+\epsilon}\hat{\mathbf{m}}_t \end{aligned} \tag{11}$$

where ϵ is a small constant for numerical stability, β_1 and β_2 are decay rates for the moment estimates, with the moments initialized to 0.

A.2 Rendering Derivation

Each 3D Gaussian $\boldsymbol{\mathcal{G}}_m$ is defined in world space by its center $\mathbf{p}_m$, scale $\mathbf{s}_m$, and rotation $\mathbf{R}_m$ (parameterized by a quaternion):

$$\boldsymbol{\mathcal{G}}_m(\mathbf{x}) = e^{-\frac{1}{2}(\mathbf{x}-\mathbf{p}_m)^\top \boldsymbol{\Sigma}_m^{-1}(\mathbf{x}-\mathbf{p}_m)} \tag{12}$$

with

$$\boldsymbol{\Sigma}_m = \mathbf{R}_m \,\mathrm{diag}(\mathbf{s}_m^2)\,\mathbf{R}_m^\top \tag{13}$$

Each Gaussian also has an opacity α_m controlling its contribution to the rendered image, and spherical harmonics coefficients $\mathbf{SH}_m$ modeling its view-dependent appearance.

Given a viewpoint $\mathcal{V}_i = (\mathbf{K}_i, \mathbf{R}_i, \mathbf{t}_i)$, the ray passing through a pixel $\mathbf{u} = (u, v)$ is expressed in camera coordinates as

$$\mathbf{x}_i(t) = \mathbf{o}_i + t\mathbf{d}_i(\mathbf{u}) \tag{14}$$

where $\mathbf{o}_i = \mathbf{0}$ is the camera origin and

$$\mathbf{d}_i(\mathbf{u}) = \frac{\mathbf{K}_i^{-1}[u, v, 1]^\top}{\|\mathbf{K}_i^{-1}[u, v, 1]^\top\|} \tag{15}$$

is the viewing direction. To render $\boldsymbol{\mathcal{G}}_m$ from viewpoint $\mathcal{V}_i$, it is first transformed into the camera coordinate frame:

$$\boldsymbol{\mu}_{m,i} = \mathbf{R}_i(\mathbf{p}_m - \mathbf{t}_i), \quad \boldsymbol{\Sigma}_{m,i} = \mathbf{R}_i \boldsymbol{\Sigma}_m \mathbf{R}_i^\top \tag{16}$$

Next, the transformed Gaussian is projected onto the image plane using a local affine approximation of the perspective projection around $\boldsymbol{\mu}_{m,i}$. The resulting 2D Gaussian footprint $\boldsymbol{\mathcal{G}}_{m,i}^{2D}$ is defined by

$$\boldsymbol{\mu}_{m,i}^{2D} = \pi(\boldsymbol{\mu}_{m,i}), \quad \boldsymbol{\Sigma}_{m,i}^{2D} = \mathbf{J}_{m,i} \boldsymbol{\Sigma}_{m,i} \mathbf{J}_{m,i}^\top \tag{17}$$

where $\mathbf{J}_{m,i}$ is the Jacobian of the projection $\pi(\cdot)$ evaluated at $\boldsymbol{\mu}_{m,i}$.

Each Gaussian $\boldsymbol{\mathcal{G}}_m$ contributes to pixel $\mathbf{u} = (u, v)$ with weight

$$w_{m,i} = \alpha_m \boldsymbol{\mathcal{G}}_{m,i}^{2D}(\mathbf{u}) \tag{18}$$

and view-dependent color $\mathbf{c}_{m,i}$ obtained by evaluating $\mathbf{SH}_m$ in the direction

$$\mathbf{v}_{m,i} = -\frac{\boldsymbol{\mu}_{m,i}}{\|\boldsymbol{\mu}_{m,i}\|} \tag{19}$$

The final pixel color is obtained via front-to-back alpha blending of all Gaussians along the ray, sorted by depth:

$$\mathbf{c}(\mathbf{u}) = \sum_{k=1}^{K} \mathbf{c}_{k,i} w_{k,i} \prod_{j=1}^{k-1} (1 - w_{j,i}) \tag{20}$$

B Initializations

We consider two scene initialization strategies. In all experiments, we use the same initialization for all compared methods to ensure that performance differences reflect the effectiveness of the optimizer rather than the initialization procedure.

ReSplat Init. When initializing a scene with the ReSplat feed-forward network [47], we run inference on the context views to produce a set of Gaussians and per-Gaussian latent state vectors derived from ReSplat's pixel-aligned features.

SfM Init. We also consider structure-from-motion (SfM) initialization using a COLMAP [2] point cloud, following the standard 3D Gaussian Splatting initialization procedure [20]. In this case, per-Gaussian latent state vectors for the learned optimizer are initialized by sampling from a standard normal distribution.

C Datasets

DL3DV [26]. A large-scale dataset for deep learning-based 3D vision with 51.2M posed frames from 10,510 videos. Testing is done on a standard 140 scenes split. For view selection within each scene, we follow the split of ReSplat [47], where context views are selected using farthest-point sampling (FPS) within a frame window, and target views are chosen evenly from the remaining frames. We use this dataset for training and testing.

RealEstate10K [52]. RealEstate10K is a large-scale dataset of real estate videos with camera poses. For evaluation, we use scenes from the official test split, subsampled by selecting every 25th scene. Scenes with an insufficient number of frames are discarded, resulting in a subset of 72 scenes over which all metrics are averaged. View selection within each scene follows the same procedure used for the DL3DV dataset. We only use this dataset at test time.

DTU [1]. We use a subset of 15 scenes commonly used for NVS from the DTU dataset, a large-scale dataset for 3D reconstruction and editing. Every 8th view is used as a target view, while the remaining views serve as context views, following the standard protocol. We only use this dataset at test time.

LLFF [35]. Dataset consisting of 8 front-facing scenes with 20 to 60 images captured handheld. Every 8th view is used as a target view, while the remaining views serve as context views, following the standard protocol. We only use this dataset at test time.

Mip-NeRF360 [4]. A dataset of 9 scenes with mixed indoor and outdoor environments, each containing more than 100 views. We downscale all scenes by a factor of 4 and use the same context/target view split as in 3DGS [20]. We only use this dataset at test time.

D Meta Training

We summarize the meta-training details in Sec. D.1. A general meta-training scheme is described in Algorithm 1. Additional details on the checkpoint buffer and the optimizer rollout strategy are provided in Section D.2. Further details on the low-visibility loss and the stability loss can be found in Sec. D.3.

D.1 Training Details

We summarize here the meta-training details for both sparse and dense settings.

Algorithm 1 Learning a 3DGS Optimizer f_θ

Input: Dataset of 3D scenes
Init: Optimizer parameters $\boldsymbol{\theta}$, meta optimizer f (Adam)
for $t_{\text{meta}} = 1, 2, \ldots$ **do**
  Sample Gaussian set $\mathcal{G}_t^j$ of a scene j
  for $t = t$ **to** $t + \tau$ **do**
    Compute inner loss gradients $\nabla_{\boldsymbol{\mathcal{G}}_t}$
    Update Gaussians: $\mathcal{G}_{t+1}^j \leftarrow \mathcal{G}_t^j - f_{\boldsymbol{\theta}}(\nabla_{\boldsymbol{\mathcal{G}}_t}, \mathcal{G}_t^j)$
  end for
  Compute meta loss gradients $\nabla_{\boldsymbol{\theta}_{t_{\text{meta}}}}$
  Update optimizer: $\boldsymbol{\theta}_{t_{\text{meta}}+1} \leftarrow \boldsymbol{\theta}_{t_{\text{meta}}} - f(\nabla_{\boldsymbol{\theta}_{t_{\text{meta}}}}, \boldsymbol{\theta}_{t_{\text{meta}}})$
end for

Dataset and splits. We train on scenes from the DL3DV dataset [26], which contains 9,896 real-world scenes with diverse environments and camera trajectories. We use the default DL3DV train/test scenes split throughout all experiments.

Dense training configuration (L2S^{D}). In the dense setting, Gaussians are initialized from SfM point clouds reconstructed using all available views, which are a free by-product of camera pose estimation and are standard in 3DGS pipelines. We observed that SfM reconstructions from DL3DV contain 10–20% of points with RGB values of exactly [0,0,0] (black), most likely an artifact of the COLMAP reconstruction. Empirically, a model trained on initializations containing these black Gaussians learns to exploit the additional representational capacity they provide. However, this leads to degraded performance when evaluated on unseen datasets that lack such points, since the assumed extra capacity is absent. For instance, fewer than 1% of initialization points are black in the MipNeRF360 dataset. Furthermore, we found that Adam struggles to recover from these uninformative Gaussians and performs substantially better when applied on filtered initializations (see also the discussion on the LLFF dataset in Sec. G.2). For these reasons, we exclude black points from training.

Latent states are randomly initialized at the start of each trajectory. For each new scene, 64 context views are selected from all available frames via furthest point sampling (FPS) to maximize scene coverage. At each inner iteration, 8 context views are sampled (also via FPS) from this fixed pool of 64. Six target views are sampled once per optimization trajectory and held fixed throughout all inner steps. Note that the SfM point cloud is reconstructed from the full set of available frames, whereas the optimizer only observes the sampled subset of context views during training. This introduces a distribution gap, as the initialization may include scene content not visible in the sampled views. To improve robustness to varying point cloud densities and this view–initialization mismatch, we apply data augmentation by randomly retaining 10–100% of the initial SfM points for each new scene, encouraging the optimizer to recover from sparse or in-

complete initializations. The augmentation range is chosen empirically such that its lower bound roughly matches the number of Gaussians observed in typical sparse initializations.

Sparse training configuration (L2S$^{\mathbf{S}}$). In the sparse-view forward-facing setting, Gaussians are initialized from the feed-forward predictions of ReSplat [47], which provides a dense initialization from a small set of posed images. Latent states are initialized from the feature vectors produced by the initialization network via a linear projection layer. At test time, when such feature vectors are unavailable (e.g., when using alternative initializations), the latent states are instead randomly initialized. For each new scene, 8 context views are sampled from a window of frames within the scene video, ensuring a relatively short baseline between views. These 8 views also serve as the input to the ReSplat initialization. Unlike the dense setting, the same fixed set of 8 context views is used across all inner optimization steps, reflecting the constrained view availability in sparse-view scenarios. Six target views are sampled once per trajectory and kept fixed during inner optimization.

Image resolution and compute. Both settings use low-resolution images (256×448 pixels) during meta-training to reduce memory consumption. All experiments are conducted in PyTorch with mixed precision (fp16/fp32) enabled. The learned optimizer is trained end-to-end for 50,000 meta-iterations on 4 NVIDIA A100 GPUs (40GB), using Adam as the meta-optimizer with a learning rate of 10^{-4}.

Gradient flow and parameterization. At each inner iteration, Gaussian parameters and their gradients are detached before being passed to the optimizer network $f_{\boldsymbol{\theta}}$, preventing direct gradient flow through the Gaussian parameters across steps. The latent state $\mathbf{s}_t$ remains fully differentiable, serving as the sole pathway for gradients to propagate between inner iterations during meta-training. This design choice reduces memory consumption during unrolling while preserving the optimizer's ability to learn long-horizon update strategies through the recurrent state.

D.2 Checkpoint Buffer and Optimizer Rollout

During meta-training, we employ a checkpoint buffer with a capacity of 20 scenes. Each scene contains the intermediate Gaussian parameters after applying t optimization steps ($\boldsymbol{\mathcal{G}}_t^j$), the optimizer state (e.g., Adam statistics), and auxiliary information required for consistent continuation across meta-iterations (e.g., scene id and total number of inner iterations applied).

At the start of each meta-iteration, the optimizer resamples a stored scene with probability $p_{\text{buffer}} = 0.7$, or samples a new scene (post initialization) with probability $1 - p_{\text{buffer}} = 0.3$. At the end of each meta-iteration, we first *rollout* the optimizer for additional inner steps without updating the meta-learner. The number of rollout steps is drawn uniformly between 1 and τ_a, where τ_a increases linearly from 1 to 50 over the first 10,000 meta iterations (i.e., the first epoch).

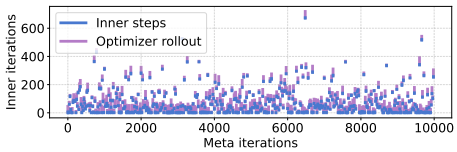


Fig. 7: Extended training horizon enabled by the checkpoint buffer and optimizer rollout (Sec. 4.3) along an entire epoch (10,000 meta iterations). Blue lines are inner iterations on which the learned optimizer is trained. Purple lines are optimizer rollouts, in which the learned optimizer is frozen.

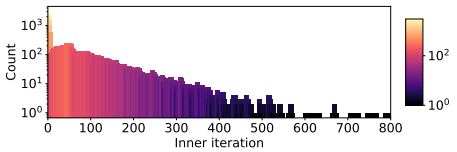


Fig. 8: Distribution of inner steps encountered by the learned optimizer during meta-training using the checkpoint buffer. If, at a given meta-iteration, the Gaussians start at inner step 20 and are updated for 6 timesteps, the range [20, ..., 25] is considered as inner steps observed once by the optimizer.

Then, the optimizer pushes the current scene to the checkpoint buffer with a probability $p_{\text{push}} = 0.99$ for new scenes and $p_{\text{push-back}} = 0.99$ for resampled scenes. If a push occurs when the buffer is already full, the oldest scene is removed from the buffer. Note that the checkpoint buffer imposes no fixed limit on the number of inner optimization steps a scene may undergo. Our configuration ensures that the meta-learner is exposed to a balanced mixture of newly sampled and replayed episodes while also observing additional simulated trajectories.

Fig. 7 shows the simulation of a single epoch of meta-training (10,000 meta-iterations). In each meta-iteration the rollout length is sampled uniformly between 1 and $\tau_a = 50$. Blue lines indicate inner iterations on which the learned optimizer is actively trained (sampled between 1 and $\tau = 6$), while purple lines denote optimizer rollouts during which the learned optimizer is frozen. As shown, the meta-learner encounters trajectories from both early and late inner timesteps (e.g., $t_{\text{inner}} = 300$) throughout the entire meta-training process, providing a more faithful representation of its eventual deployment on novel scenes.

Fig. 8 further shows the distribution of inner timesteps sampled during a single meta-epoch. "Trained" timesteps (1-6) appear approximately 1,000 times out of the 10,000 meta-iterations, as optimization at these early stages varies more across scenes. Moreover, as the scene is close to initialization, the meta-optimizer typically predicts larger updates. As shown in Figs. 10 and 16, L2S^{S} reaches 90% of its final PSNR early in the inner optimization. Nevertheless, exposure to later, near-saturated timesteps is crucial for robustness across different optimization regimes. Together with the architecture and loss formulation described in Sec. 4, this enables the meta-optimizer to perform stable and effective updates even in late-stage optimization. For completeness, we provide pseudo-code for the checkpoint-buffer algorithm in Algorithm 2.

D.3 Losses

Low-Visibility Loss. As discussed in Section 4.1, Gaussians with low visibility receive only weak supervision from the rendering loss. To mitigate this,

Algorithm 2 Checkpoint Buffer Training for a Learned Optimizer in 3DGS

Init: Checkpoint buffer $\mathcal{B} \leftarrow \emptyset$
Input: Learned optimizer f_θ; probabilities p_{buffer}, p_{push}, $p_{\text{push-back}}$, τ_{inner}, τ_a
for each meta-iteration t_{meta} **do**
  `# Sample new scene or from buffer`
  $\boldsymbol{\mathcal{G}}^j_{t_{\text{inner}}} \leftarrow \begin{cases} \text{Sample}(\mathcal{B}) & \text{if rand}() < p_{\text{buffer}} \text{ and } \mathcal{B} \neq \emptyset \\ \text{Initialize}() & \text{otherwise} \end{cases}$
  `# Inner optimization`
  $\tau \leftarrow U(1, \tau_{\text{inner}})$
  for $t = t_{\text{inner}}$ **to** $t_{\text{inner}} + \tau$ **do**
    $\boldsymbol{\mathcal{G}}^j_t \leftarrow \text{Update}(\boldsymbol{\mathcal{G}}^j_{t-1}, f_{\boldsymbol{\theta}})$
  end for
  Update optimizer parameters $\boldsymbol{\theta}_{t_{\text{meta}}}$ with accumulated loss
  `# Optimizer rollout`
  $\tau_{\text{rollout}} \leftarrow U(1, \tau_a)$
  for $t = t_{\text{inner}} + \tau$ **to** $t_{\text{inner}} + \tau + \tau_{\text{simulate}}$ **do**
    $\boldsymbol{\mathcal{G}}^j_t \leftarrow \text{Update}(\boldsymbol{\mathcal{G}}^j_{t-1}, f_{\boldsymbol{\theta}}))$
  end for
  `# Push to buffer`
  $\text{Push}(\mathcal{B}, \boldsymbol{\mathcal{G}}^j_t, p_{\text{push}} \text{ if } \boldsymbol{\mathcal{G}}^j_{t_{\text{inner}}} \text{ new else } p_{\text{push-back}})$
end for

we introduce a per-parameter *low-visibility* loss. For clarity, we describe the loss for a single Gaussian out of the G Gaussians in the scene. For each Gaussian parameter update $\boldsymbol{\Delta}_{\boldsymbol{\mathcal{G}}_t} \in \mathbb{R}^{59}$, with its corresponding raw gradient (before normalization) $g \in \mathbb{R}^{59}$ and normalized Adam-style gradient $\nabla_{\boldsymbol{\mathcal{G}}_t} \in \mathbb{R}^{59}$, we impose a penalty on parameter i whenever one of the following conditions holds:
(i) **Vanishing gradient:** the gradient magnitude is *extremely* small:

$$|g_i| < \varepsilon, \qquad \varepsilon = 10^{-8} \tag{21}$$

(ii) **Sign disagreement:** the predicted update direction disagrees with that of the normalized Adam gradient:

$$\text{sign}(\boldsymbol{\Delta}_{\boldsymbol{\mathcal{G}}_t,i}) \neq \text{sign}(\nabla_{\boldsymbol{\mathcal{G}}_t,i}) \tag{22}$$

We define a binary mask for each parameter as

$$m_i = \mathbf{1}\Big[\, |g_i| < \varepsilon \;\; \vee \;\; \text{sign}(\boldsymbol{\Delta}_{\boldsymbol{\mathcal{G}}_t,i}) \neq \text{sign}(\nabla_{\boldsymbol{\mathcal{G}}_t,i}) \Big] \tag{23}$$

and express the low-visibility loss in vector form for a single Gaussian as:

$$\mathcal{L}_{\text{lvs}} = \sum_{i=1}^{59} m_i \, |\boldsymbol{\Delta}_{\boldsymbol{\mathcal{G}}_t,i}| \tag{24}$$

This applies an ℓ_1 penalty exclusively to parameters that satisfy the low-visibility conditions, thereby providing explicit feedback to the meta-optimizer on how to

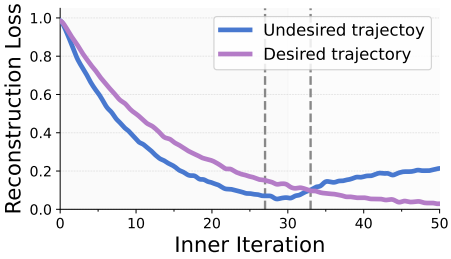


Fig. 9: Mitigating Optimization Degradation via Stability Constraints. Within a meta-iteration (dashed lines), the blue trajectory achieves a lower instantaneous loss than the purple one even though it has already entered a degraded regime that will lead to worse reconstructions later. Relying solely on absolute reconstruction error would incorrectly favor this unstable path. The stability loss instead penalizes local increases in error, promoting the more robust, consistently improving trajectory shown in purple.

update parameters that would otherwise receive weak or inconsistent gradient signals.

Stability loss. The stability loss addresses a common failure mode where learned optimizers discover "shortcuts" that yield a low instantaneous error but lead to long-term divergence. In practice, an optimizer may exploit local minima by overfitting to current views or prematurely optimizing higher-order spherical harmonics. As illustrated in Fig. 9, evaluating progress based only on ground-truth loss at a fixed point fails to distinguish these unstable spikes from sustainable improvement. By penalizing increases in reconstruction error between consecutive inner iterations, this loss term encourages the discovery of update directions that maintain consistent optimization behavior over time.

E Architectural Details

This section provides additional architectural details of our learned optimizer.

kNN-based Point Transformer. The *kNN-based Point Transformer* branch begins with a linear layer $[374, 256]$, followed by four sequential Transformer blocks. Each block applies LayerNorm to its input and performs k-nearest neighbors (kNN) attention over the 3D point cloud of Gaussian means. In each kNN attention layer, the 256-dim input is linearly mapped to 192 dimensions and split into query, key, and value vectors of 64 dimensions each. Attention is computed for each Gaussian using its k nearest neighbors, yielding a 64-dim output per point, which is then projected back to 256 dimensions via a linear layer $[64, 256]$. The attention output and the block input are combined via a residual (skip) connection before being passed through LayerNorm and an MLP consisting of two linear layers $[256, 1024]$ and $[1024, 256]$, with a GeLU activation in between,

followed by a second skip connection. The output of the final Transformer block produces the updated Gaussian states $\mathbf{s}_{t+1}$ before scaling.

We analyze the kNN scalability in a controlled setup with varying numbers of primitives ($G \in [10^4, \ldots, 10^7]$). Memory scales linearly with G, while runtime scales approximately as $G^{1.7}$, slightly below the worst-case theoretical complexity. Following ReSplat, we initially use $k = 16$ neighbors, which accounts for 28% of the inner-step runtime. Ablating k shows it can be reduced to 4, lowering total runtime by 15.7% without affecting quality; our final models therefore use $k = 4$. Finally, for additional efficiency, we run the kNN operation only every 100 optimization iterations at test time.

State Scale MLP. The *State Scale MLP* is as a lightweight network consisting of two linear layers $[374, 187]$ and $[187, 1]$, each followed by a ReLU activation.

Update MLP. The *Update MLP* includes two linear layers $[256, 60]$ and $[60, 60]$, with a GeLU activation in between. The first 59 elements of each latent state are normalized to unit length. The last element is activated with ReLU and represents a learned update scaling factor.

F Baselines

F.1 3DGS

For the 3DGS baseline, we use the Adam optimizer with separate learning rates for each group of parameters, as in the original implementation [20] (see Table 1). The learning rate for the Gaussian means is scaled based on the number of optimization steps performed (log-linear interpolation). Adam's betas hyper-parameters are kept at their default values ($\beta_1 = 0.9, \beta_2 = 0.999$). Unlike the standard setting, we always use a batch size of 8 views for rendering and loss computation. In the sparse setting this corresponds to using all available views at each iteration, while in the dense setting we sample a different set of views at each iteration. Adaptive density control is not applied.

Parameter	LR
means (init)	1.6e-4
means (final)	1e-5
scales	5e-3
rotations	1e-3
opacities	5e-2
sh0s	2.5e-3
shNs	1.25e-4

Table 1: Learning rates used for the 3DGS baseline.

F.2 3DGS*

We perform a grid search over the learning rates and Adam optimizer parameters using 10 scenes from the DL3DV test set, rendered at low resolution with 8 views per scene and ReSplat initialization (corresponding setup as Fig. 10(a)). We find that the best-performing learning rates are approximately 5× larger than those listed in Table 1, with no decay applied to the mean learning rate. The optimal Adam hyper-parameters are $\beta_1 = 0.99$ and $\beta_2 = 0.999$. These values are used in all experiments that reference 3DGS*.

F.3 ReSplat

For the ReSplat [47] baseline, we use the implementation and pretrained weights of the original paper. We use the 8 views, low resolution setting, matching the training of L2S$^{\mathbf{S}}$.

F.4 LO Baseline

As discussed in Section 5.2, we implement a learned optimizer (LO) baseline that incorporates the cosine LR scheduler from [14] and the time positional encoding used in [14, 29]. We use the same SH dimensionality as in our experiments. The LO baseline employs the *ReSplat* network architecture, including Adam-style gradient computations. Importantly, it does not include our additional losses or the state and update scaling mechanisms introduced in our method. The model is trained in the same sparse setting as L2S$^{\mathbf{S}}$, but with the same meta-learning procedure as G3R.

With this baseline, we establish a *fair and controlled reference* for evaluating the impact of our proposed modifications, particularly the incorporation of $\mathcal{L}_{\text{lvs}}$ and the state/update scaling mechanisms. It shows that the auxiliary mechanisms used in prior works only partially mitigate degradation of the learned optimizer optimization and are unable to fully solve the issue across different training horizons.

Time Positional Encoding. The LO baseline uses the time encoding from [14, 29], which encodes the iteration step t as a higher-dimensional vector using frequency positional encoding, following standard practice [36, 40]:

$$\gamma(p) = \left(\sin\left(2^k \pi p\right), \cos\left(2^k \pi p\right)\right)_{k=0}^{L-1} \tag{25}$$

where $L = 6$.

Learning Rate Scheduler. The baseline employs the DDPM cosine learning rate scheduler [37], following [14]. The learning rate at step t is

$$\eta_t = \eta_{\min} + (\eta_{\max} - \eta_{\min}) \cos\left(\frac{t/T + s}{1 + s} \cdot \frac{\pi}{2}\right)^2 \tag{26}$$

where $\eta_{\max} = 1$ and $\eta_{\min} = 0$ denote the initial and minimum learning rates, respectively, and T denotes the total number of training steps. We use the default offset $s = 0.008$. This schedule allows for large updates early in training and gradual decay as optimization progresses.

For the LO baseline, we follow the training setup of G3R: the learned optimizer is updated at every inner iteration during meta-training, using 24 inner steps. This differs from our approach, which aggregates information across multiple inner iterations before performing an update. We set $T = 100$ for the maximum timestep to match the value used during inference in G3R. For experiments requiring longer horizons, we set T accordingly. For example, $T = 2000$ in the DL3DV experiments.

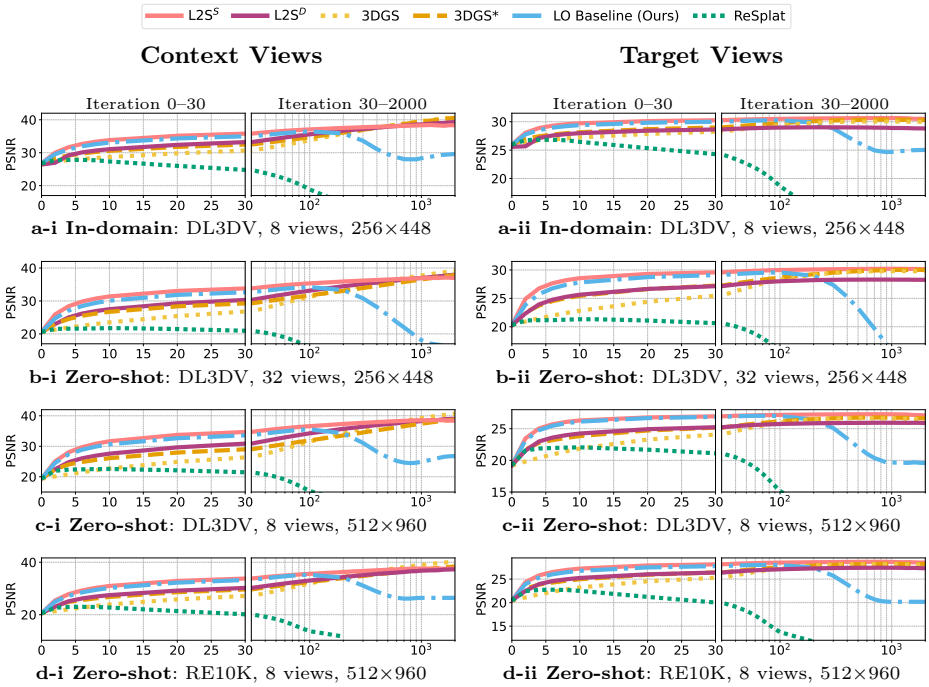


Fig. 10: Quantitative Results on ReSplat Init., Sparse Setting: DL3DV and RE10K. PSNR optimization trajectories on **context** (left column) and **target** (right column) views. See Sec. G.1 for discussion.

G Additional Results

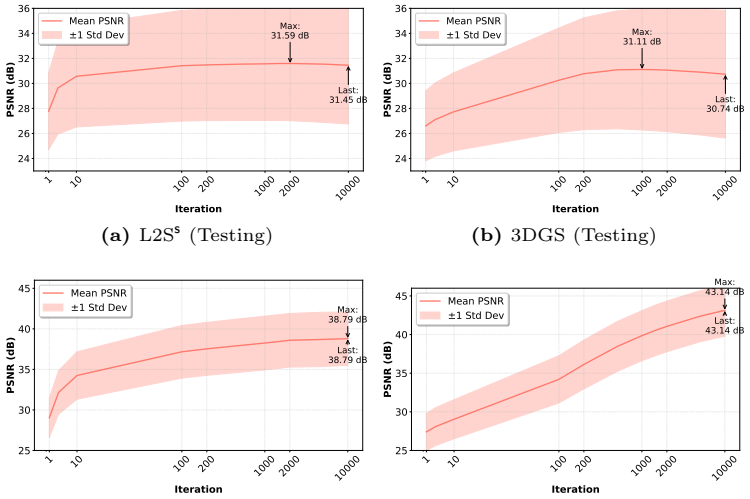
We provide additional generalization results in the sparse (Sec. G.1) and dense settings (Sec. G.2).

G.1 Sparse setting

We further evaluate the zero-shot generalization of L2S^{S} and L2S^{D} across different datasets, resolutions, and numbers of views in the sparse setting. For each experiment, we report PSNR on both context and target views throughout the inner optimization. We consider four configurations:

- In domain: DL3DV with 8 views at low resolution (Figs. 10a-i and 10a-ii and Tab. 2a).
- DL3DV with 32 views at low resolution (Figs. 10b-i and 10b-ii and Tab. 2b).
- DL3DV with 8 views at high resolution (Figs. 10c-i and 10c-ii and Tab. 2c).
- RE10K with 8 views at high resolution (Figs. 10d-i and 10d-ii and Tab. 2d).

For completeness, we include results reported in the main paper (Figs. 4(a) and 4(b)). We compare learned and non-learned optimizers initialized from the



(a) L2S^{s} (Testing) **(b)** 3DGS (Testing)

(c) L2S^{s} (Training) **(d)** 3DGS (Training)

Fig. 11: PSNR Comparison. Testing (top row) and training (bottom row) views between L2S^{s} (left) and 3DGS (right). Values are computed over 10 scenes from the DL3DV test set in the sparse low-resolution setting (8 views, 256×448 resolution).

feed-forward predictions of ReSplat [47], which produces approximately 230K primitives at high resolution and 57K primitives at low resolution. In all experiments, all methods use all available views at each iteration and are run for a total of 2000 iterations. In addition, Fig. 15 compares L2S^{s} and L2S^{d} on one DL3DV scene under both ReSplat and sparse SfM initialization (reconstructed from the available input views). Tab. 2 summarizes the iteration and runtime efficiency of all methods across these evaluation settings.

Target-view performance. Fig. 10 shows trends consistent with those observed in the main paper on the testing views (Figs. 4(a) and 4(b)). Across all configurations, L2S^{s} reaches the final quality of 3DGS* earlier during optimization while also achieving a higher final PSNR than both 3DGS variants. The gap becomes larger in the denser-view configuration (32 views) and in the high-resolution DL3DV setting. The early optimization gains also translate into improved wall-clock time efficiency (See Sec. G.3 and Fig. 16). As discussed in the main paper, L2S^{d} also achieves higher PSNR early in the optimization, but saturates at a lower final PSNR than the 3DGS variants.

Among the classical optimizers, the tuned learning rate of 3DGS* consistently outperforms the default learning rate used in 3DGS [20] in the sparse setting. The LO baseline initially follows the behavior of L2S^{s} but begins to deviate after approximately 100 iterations when applied beyond its trained optimization horizon. During training, the optimizer is unrolled for 24 steps, while the learning-rate schedule is stretched to 100 steps to match the training and inference setup of G3R [14]. When applied to longer horizons at test time (e.g., the

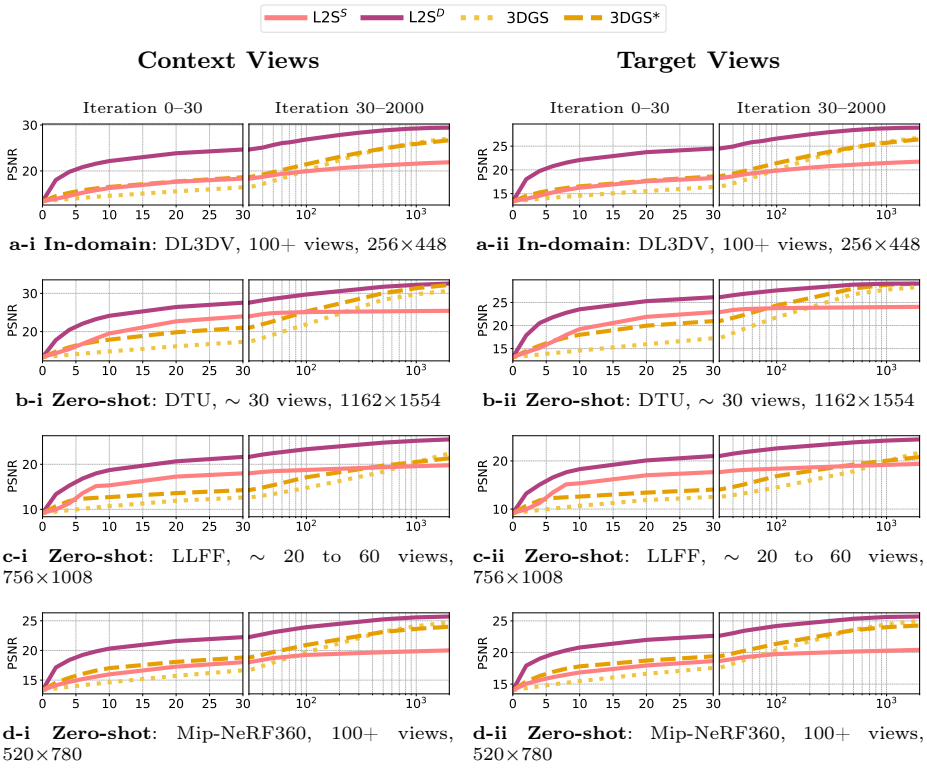


Fig. 12: Quantitative Results on SfM Init., Dense Setting: DL3DV, DTU, LLFF and Mip-NeRF360. PSNR optimization trajectories on **context** (left column) and **target** (right column) views. See Sec. G.2 for discussion.

32-view configuration requires roughly 300 iterations to match the performance of 3DGS*), the learning-rate schedule must be stretched accordingly, producing update trajectories that were not encountered during training and are no longer consistent with the model's time encoding. As a result, the LO baseline gradually deviates from the desired optimization behavior beyond its trained range.

ReSplat improves during the very early iterations but subsequently degrades. Note that ReSplat was trained in the same sparse setting as L2S$^{\mathbf{S}}$ and is therefore also evaluated in a zero-shot manner.

Context-view performance. The behavior on context views (Fig. 10-i) reveals a clear difference between learned and non-learned optimization strategies. For the 3DGS variants, PSNR on the context views continues to increase even after the performance on the target views has saturated, suggesting overfitting to the training views. In contrast, L2S$^{\mathbf{S}}$ exhibits more moderate improvements on the context views. This behavior is consistent with the meta-training objective, which includes a loss on the *target views* and therefore discourages overfitting

to the context observations. We illustrate this by optimizing 10 scenes from the DL3DV test set in the sparse, low-resolution setup for 10,000 iterations, as shown in Fig. 11. While Adam continues to improve performance on the training views, its testing performance degrades by approximately 0.37 dB. In contrast, L2S$^{\mathbf{S}}$ maintains a small improvement on the training set while exhibiting a smaller degradation on the testing set (0.14 dB). Overall, our method outperforms Adam by approximately 0.4 dB after iteration 1,000 and converges faster (larger gap in earlier iterations).

G.2 Dense setting

We further evaluate the zero-shot generalization of L2S$^{\mathbf{S}}$ and L2S$^{\mathbf{D}}$ across different datasets, resolutions, and numbers of views in the dense setting. For each experiment, we report both context and target views PSNR values across the inner optimization iterations. We consider four configurations:

- In domain: DL3DV with all views at low resolution (Figs. 12a-i and 12a-ii and Tab. 3a).
- DTU with ~ 30 views at high resolution (Figs. 12b-i and 12b-ii and Tab. 3b).
- LLFF with $\sim$ 20 to 60 views at high resolution (Figs. 12c-i and 12c-ii and Tab. 3c).
- Mip-NeRF360 with 100+ views at high resolution (Figs. 12d-i and 12d-ii and Tab. 3d).

For completeness, we include results reported in the main paper (Figs. 4(c) to 4(f)). We compare learned and non-learned optimizers initialized from SfM, with variable number of primitives per scene. In all experiments, all methods use a different subset of 8 views at each iteration and are run for a total of 2000 iterations. Tab. 3 and Fig. 17 summarize the iteration and runtime efficiency of all methods across these evaluation settings.

Compared to the sparse setting, the image quality gap between context and target views is much smaller. This may be explained by the stronger constraints imposed by the denser multi-view supervision, which reduce overfitting to the context views.

LLFF Results Comments. The LLFF dataset, as originally released, contains COLMAP reconstructions where many points are incorrectly assigned black colors. As a result, the SfM initialization used in the main paper (and in Figs. 12c-i, 12c-ii and 14 and Tab. 3c) contains a large number of black Gaussians, and in some scenes almost exclusively so. Although we filter out such points during training on the DL3DV dataset (see Sec. D.1), L2S$^{\mathbf{D}}$ can recover from these uninformative Gaussians, whereas Adam struggles. This results in a larger PSNR gap in favor of our method compared to the best-performing 3DGS configuration (2–3 dB). We hypothesize that our optimizer recovers from such poor initializations faster than Adam, which progresses through smaller updates. After recoloring the point clouds by reassigning point colors via projection onto image planes and taking the median color across observations, the final PSNR gap reduces to approximately 0.35 dB.

G.3 Timings

To assess optimization efficiency, we report the number of iterations and wall-clock time that L2S$^{\mathbf{S}}$ and L2S$^{\mathbf{D}}$ required to reach a given percentage of the average PSNR gain (from initialization to the final 3DGS [20] or 3DGS* values). We report these results in Figs. 16 and 17. Across the evaluated settings, the corresponding model (L2S$^{\mathbf{S}}$ or L2S$^{\mathbf{D}}$) reaches all thresholds with fewer iterations and lower wall-clock time than the 3DGS baselines.

H Analysis of L2S$^{\mathbf{S}}$

H.1 Statistical Analysis

In Fig. 18 we show the average norm of the updates for each group of parameters over 10,000 optimization steps for 10 scenes from the DL3DV test set. We report the update norms for both 3DGS with the Adam optimizer and our learned optimizer in Fig. 18(a). As can be seen, the magnitudes of the updates are much larger during the early iterations, when our learned optimizer achieves its performance advantage over Adam, and gradually decay to zero as the optimization converges. Figure 18(c) further illustrates the decay of the internal state of the learned optimizer. Results are computed over 10 scenes from the DL3DV test set in the sparse low-resolution setting (8 views, 256×448 resolution).

H.2 Per Parameter Contribution

In this section, we present an analysis of how each parameter group contributes to the behavior of Adam (3DGS [20]) and L2S$^{\mathbf{S}}$ during optimization. Fig. 19 compares how optimization progresses when individual parameter groups are selectively included or excluded during training. For both Adam (Fig. 19(a)) and L2S$^{\mathbf{S}}$ (Fig. 19(b)), each subplot isolates a single parameter: means, scales, quaternions, opacities, the first SH channel (sh0), and the remaining SH channels (shN), and evaluates four conditions: updating all parameters, freezing only that parameter group, updating only that parameter group, and performing no updates. Note that although L2S$^{\mathbf{S}}$ now updates each parameter independently (or excludes different parameters), it was trained to *jointly* update all parameters. All of the experiments were conducted on 10 scenes of DL3DV test set in the sparse low resolution.

Across all parameters and across both optimizers, the “All" configuration reliably yields the fastest PSNR improvement, confirming that none of the parameter updates introduce negative effects. For Adam, scales emerge as the most influential parameter: removing them noticeably slows convergence, while optimizing only the scales brings significant improvements. Opacities, sh0, and shN have little impact when removed, though optimizing only these groups still yields slight improvements over the no-update baseline. For L2S$^{\mathbf{S}}$, opacities and sh0 have little influence, whereas the means and shN contribute substantially. Removing the latter severely degrades convergence, and optimizing only these

Optimizer		Best PSNR↑	Best SSIM↑	Best LPIPS↓	At 3DGS* PSNR Iter↓	At 3DGS* PSNR Time (s)↓
MVSplat Init† [13]		24.16	0.82	0.17	–	–
DepthSplat Init† [48]		25.81	0.86	0.13	–	–
ReSplat Init† [47]		25.96	0.85	0.14	–	–
WorldMirror Init† [28]		23.54	0.79	0.18	–	–
3DGS [20]	SfM	20.80	0.64	0.46	–	–
	RS	30.05	0.91	0.08	–	–
3DGS*	SfM	20.29	0.61	0.47	–	–
	RS	30.36	0.92	0.07	900	7.7
ReSplat‡ [47]	RS	26.82	0.86	0.11	–	–
LO Baseline‡	SfM	19.91	0.59	0.49	–	–
	RS	30.25	0.92	0.07	–	–
L2S^{S}‡	SfM	19.34	0.56	0.53	–	–
	RS	30.65	0.92	0.07	43	1.3
L2S^{D}‡	SfM	21.82	0.67	0.43	–	–
	RS	29.02	0.90	0.09	–	–

(a) In-domain: DL3DV, 8 views, 256 × 448.

Optimizer		Best PSNR↑	Best SSIM↑	Best LPIPS↓	At 3DGS* PSNR Iter↓	At 3DGS* PSNR Time (s)↓
MVSplat Init† [13]		16.42	0.53	0.46	–	–
DepthSplat Init† [48]		16.83	0.55	0.43	–	–
ReSplat Init† [47]		20.28	0.71	0.26	–	–
WorldMirror Init† [28]		OOM	OOM	OOM	–	–
3DGS [20]	SfM	–	–	–	–	–
	RS	29.80	0.91	0.08	–	–
3DGS*	SfM	–	–	–	–	–
	RS	30.02	0.91	0.07	1600	73.0
ReSplat‡ [47]	RS	21.32	0.74	0.22	–	–
LO Baseline‡	SfM	–	–	–	–	–
	RS	29.56	0.91	0.08	–	–
L2S^{S}‡	SfM	–	–	–	–	–
	RS	30.21	0.91	0.07	133	18.8
L2S^{D}‡	SfM	–	–	–	–	–
	RS	28.31	0.89	0.10	–	–

(b) Zero-shot: DL3DV, 32 views, 256 × 448.

Optimizer		Best PSNR↑	Best SSIM↑	Best LPIPS↓	At 3DGS* PSNR Iter↓	At 3DGS* PSNR Time (s)↓
MVSplat Init† [13]		19.01	0.63	0.42	–	–
DepthSplat Init† [48]		20.25	0.67	0.35	–	–
ReSplat Init† [47]		19.19	0.62	0.37	–	–
WorldMirror Init† [28]		17.60	0.51	0.40	–	–
3DGS [20]	SfM	–	–	–	–	–
	RS	26.64	0.84	0.15	–	–
3DGS*	SfM	–	–	–	–	–
	RS	26.77	0.85	0.15	700	21.8
ReSplat‡ [47]	RS	22.06	0.72	0.28	–	–
LO Baseline‡	SfM	–	–	–	–	–
	RS	27.04	0.85	0.14	25	5.8
L2S^{S}‡	SfM	–	–	–	–	–
	RS	27.28	0.85	0.14	20	2.5
L2S^{D}‡	SfM	–	–	–	–	–
	RS	25.94	0.82	0.16	–	–

(c) Zero-shot: DL3DV, 8 views, 512 × 960.

Optimizer		Best PSNR↑	Best SSIM↑	Best LPIPS↓	At 3DGS* PSNR Iter↓	At 3DGS* PSNR Time (s)↓
MVSplat Init† [13]		–	–	–	–	–
DepthSplat Init† [48]		–	–	–	–	–
ReSplat Init† [47]		–	–	–	–	–
WorldMirror Init† [28]		–	–	–	–	–
3DGS [20]	SfM	–	–	–	–	–
	RS	28.13	0.88	0.13	–	–
3DGS*	SfM	–	–	–	–	–
	RS	28.24	0.89	0.12	1000	29.7
ReSplat‡ [47]	RS	22.75	0.79	0.21	–	–
LO Baseline‡	SfM	–	–	–	–	–
	RS	28.01	0.89	0.12	–	–
L2S^{S}‡	SfM	–	–	–	–	–
	RS	28.68	0.89	0.11	38	5.0
L2S^{D}‡	SfM	–	–	–	–	–
	RS	27.42	0.88	0.13	–	–

(d) Zero-shot: RE10K, 8 views, 512 × 960.

Table 2: Quantitative Evaluation on Sparse Setting. Results on DL3DV [26] and RealEstate10K [52] (RE10K) datasets. † feed-forward methods. ‡ learned optimizer methods. In addition to ReSplat initialization (RS), we also evaluate SfM initialization in the setting where it is available (Fig. 15). The COLMAP reconstruction uses only the 8 context views, avoiding any information leakage from target views. This results in 1–10k points per scene, making it a much sparser initialization. L2S^{S} (RS) initializes per-Gaussian latent state vectors using ReSplat's pixel-aligned features. All other configurations of L2S^{S} and L2S^{D} initialize per-Gaussian latent state vectors as sampled from a standard normal distribution. **Left:** Best metrics achieved along the optimization trajectory. **Right:** Iteration to reach 3DGS* max PSNR with ReSplat initialization; "–" indicates never reached. **In-domain** results match our L2S^{S} training configuration (dataset, number of views, and resolution), while **zero-shot** results differ in at least one of these factors. Results are linear interpolated between discrete evaluation timestep, to achieve the iteration in which the target PSNR was reached. We highlight the best, second best, and third best results. See Sec. G.1 for discussion.

Method	Best PSNR↑	SSIM↑	LPIPS↓	At 3DGS PSNR Iter↓	Time (s)↓
3DGS [20]	26.76	0.86	0.21	2000	18.3
3DGS*	26.43	0.85	0.23	–	–
L2S^{D}	28.89	0.90	0.16	119	2.9
L2S^{S}	21.74	0.71	0.39	–	–

(a) In-domain: DL3DV [26], 100+ views, 256 × 480.

Method	Best PSNR↑	SSIM↑	LPIPS↓	At 3DGS PSNR Iter↓	Time (s)↓
3DGS [20]	28.37	0.89	0.32	2000	26.7
3DGS*	29.11	0.89	0.33	709	8.5
L2S^{D}	29.10	0.89	0.32	341	7.3
L2S^{S}	24.05	0.79	0.43	–	–

(b) Zero-shot: DTU [1], ∼ 30 views, 1162×1554.

Method	Best PSNR↑	SSIM↑	LPIPS↓	At 3DGS PSNR Iter↓	Time (s)↓
3DGS [20]	21.74	0.70	0.40	2000	32.5
3DGS*	20.79	0.65	0.46	–	–
L2S^{D}	24.47	0.77	0.31	48	1.3
L2S^{S}	19.38	0.60	0.52	–	–

(c) Zero-shot: LLFF [35], ∼ 20 to 60 views, 756×1008.

Method	Best PSNR↑	SSIM↑	LPIPS↓	At 3DGS PSNR Iter↓	Time (s)↓
3DGS [20]	25.00	0.70	0.39	2000	53.6
3DGS*	24.27	0.66	0.44	–	–
L2S^{D}	25.69	0.72	0.37	382	17.6
L2S^{S}	20.42	0.53	0.57	–	–

(d) Zero-shot: Mip-NeRF360 [4], 100+ views, 520 × 780.

Table 3: Quantitative Evaluation on Dense Datasets. All methods are initialized with SfM initialization. Both L2S^{S} and L2S^{D} initialize each Gaussian's latent state vector by sampling from a standard normal distribution. Conditioning gradients are computed for a subset of 8 views sampled at each iteration with furthest point sampling from the training views set. This matches the training configuration of L2S^{D}. **Left:** Maximum image quality metrics. **Right:** Iteration at which each method reached the maximum PSNR of 3DGS; "–" indicates that the method never reached that value. **In-domain** results match our L2S^{D} training configuration (dataset, number of views, and resolution), while **zero-shot** results differ in at least one of these factors. Results are linear interpolated between discrete evaluation timestep, to achieve the iteration in which the target PSNR was reached. We highlight the best, second best and third best results. See Secs. 5.2 and G.2 for discussion.

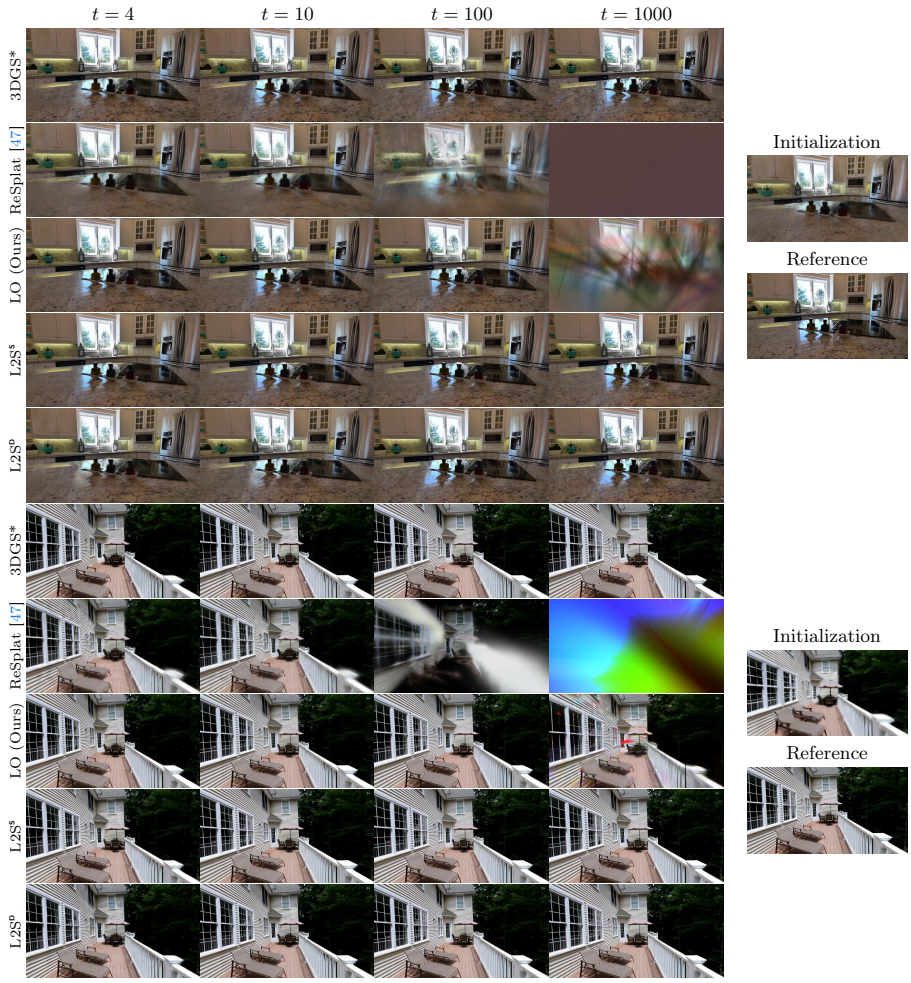


Fig. 13: Zero-shot Generalization to RealEstate10k. Scene reconstructions from RealEstate10K [52] in the 8 views, zero-shot high resolution setting (512×960).

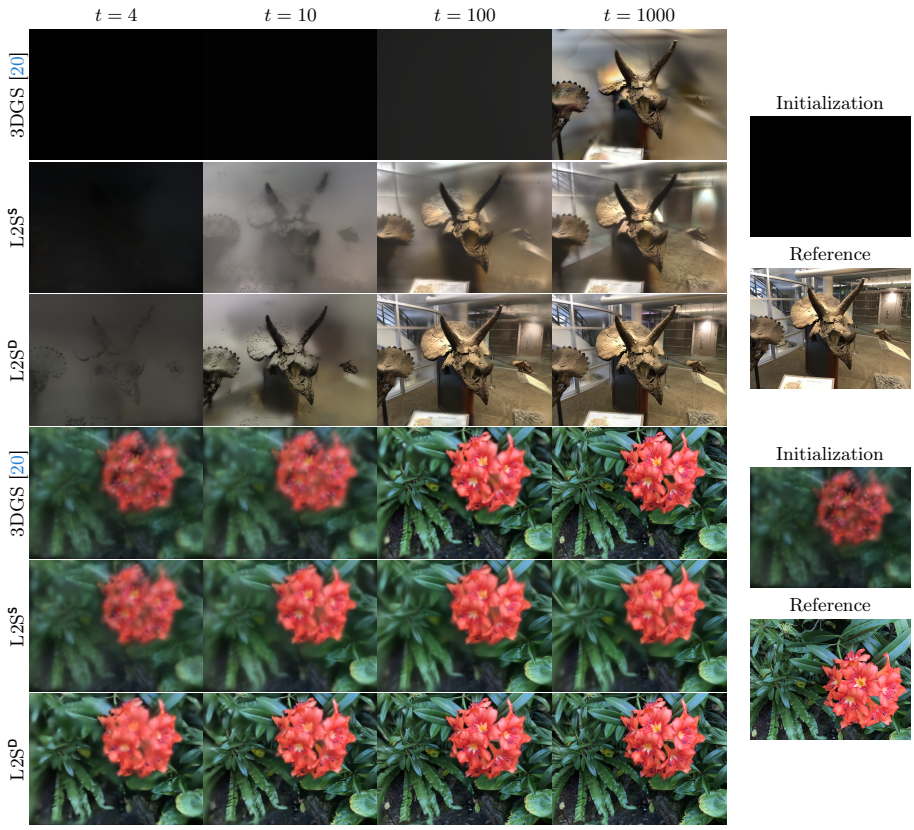


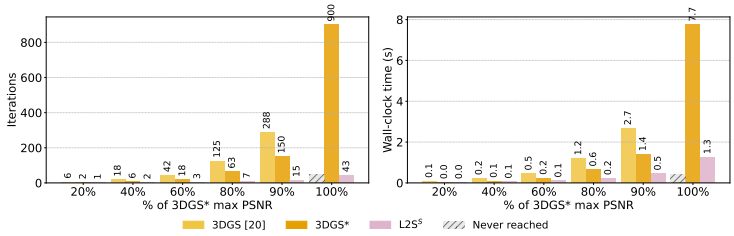
Fig. 14: Zero-shot Generalization to LLFF. Scene reconstructions from LLFF [35] in the $\sim$ 20 to 60 views, zero-shot high-resolution setting (756×1008). We discuss the black SfM initialization, resulting from the original COLMAP reconstruction provided with the dataset, in Sec. G.2.



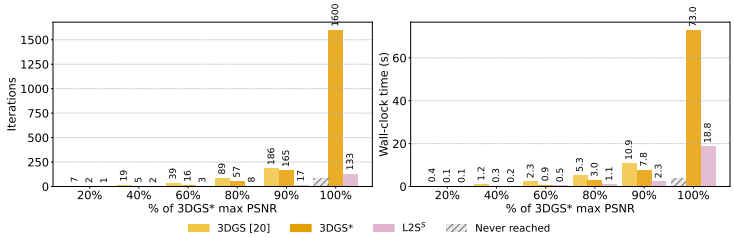
(a) ReSplat initialization

(b) SfM initialization

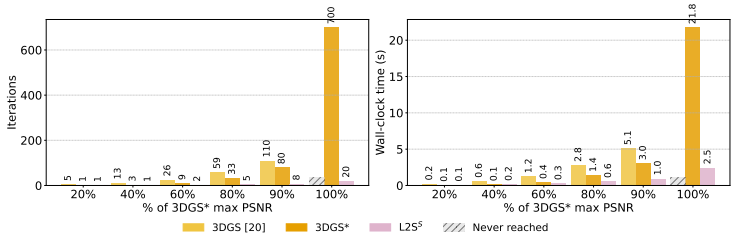
Fig. 15: Initializations Comparison. Scene reconstructions from DL3DV [26] sparse setting, 8 views, low-resolution (256×448). Note that ReSplat produces 57,344 Gaussians, while the sparse SfM initialization yields only 810 points. Under this extreme setting, L2S$^{\mathbf{D}}$, which was trained with random dropping of initialization points, outperforms 3DGS* at recovering details from a very low-capacity representation. Interestingly, L2S$^{\mathbf{S}}$, trained only from dense initializations, performs worse. We also note that no adaptive density control is used, as we compare raw optimizer performance on fixed capacity representations. Final PSNR results reflect this trend. With ReSplat initialization, 3DGS* reaches 26.83 dB, L2S$^{\mathbf{S}}$ 27.66 dB, and L2S$^{\mathbf{D}}$ 25.63 dB. With SfM initialization, performance drops overall, with 3DGS* at 20.40 dB, L2S$^{\mathbf{S}}$ at 20.46 dB, and L2S$^{\mathbf{D}}$ achieving the best result at 22.21 dB.



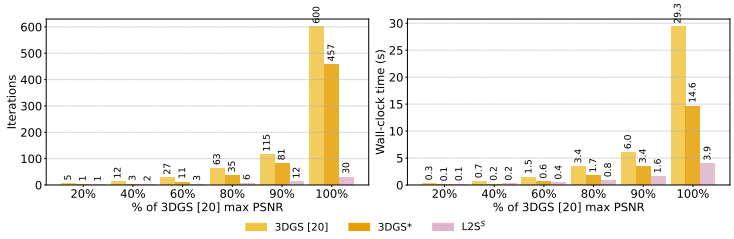
(a) DL3DV [26], 8 views, 256 × 480.



(b) DL3DV [26], 32 views, 256 × 480.

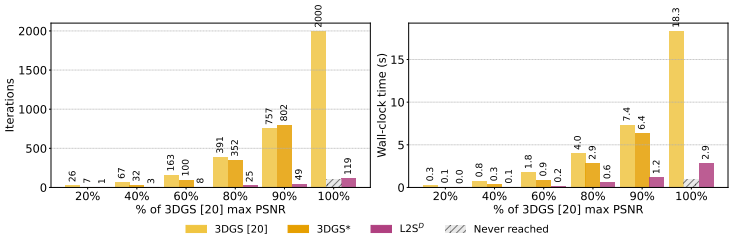


(c) DL3DV [26], 8 views, 512 × 960.

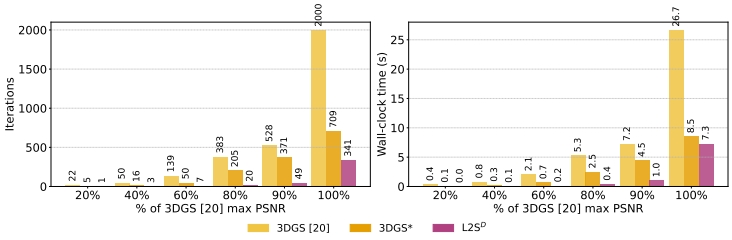


(d) RealEstate10K [52], 8 views, 512 × 960.

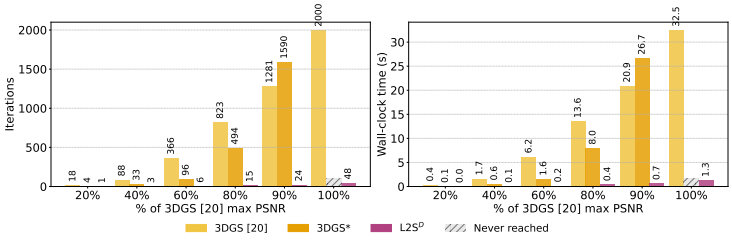
Fig. 16: Optimization timing. We average the PSNR curves across scenes and measure the iterations (left) and wall-clock time (right) required to reach a given percentage of the average PSNR gain (from initialization to the final 3DGS* value). A hatched bar indicates the threshold was never reached. Our method (L2S^S, light purple) consistently reaches all thresholds with substantially fewer iterations and less wall-clock time than both 3DGS baselines, highlighting faster improvement in early stages.



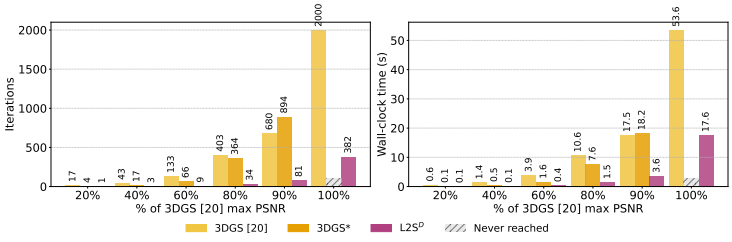
(a) DL3DV [26], 100+ views, 256 × 480.



(b) DTU [1], ∼ 30 views, 1162 × 1554.



(c) LLFF [35], 20 − 60 views, 756 × 1008.



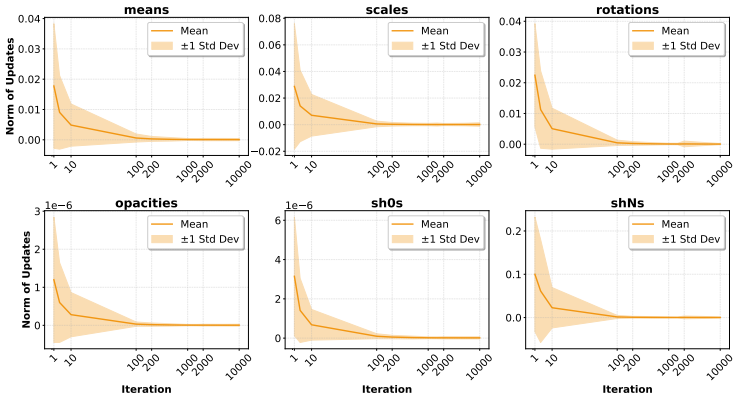
(d) Mip-NeRF360 [4], 100+ views, 520 × 780.

Fig. 17: Optimization timing. We average the PSNR curves across scenes and measure the iterations (left) and wall-clock time (right) required to reach a given percentage of the average PSNR gain (from initialization to the final 3DGS [20] value). A hatched bar indicates the threshold was never reached. Our method (L2S$^{\mathbf{D}}$, purple) consistently reaches all thresholds with fewer iterations and less wall-clock time than the 3DGS baseline, demonstrating faster early convergence. The speedups to reach the maximum 3DGS PSNR are 6.4× on DL3DV, 3.6× on DTU, 24.6× on LLFF, and 3.1× on Mip-NeRF360.

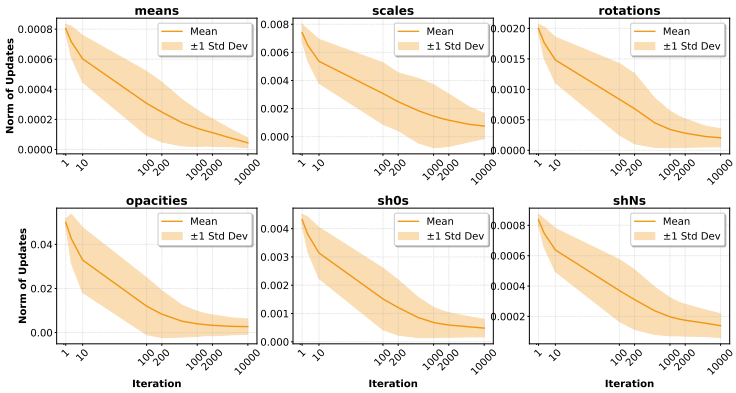
parameters yields clear gains. Since excluding opacities and sh0 does not reduce the maximum PSNR in these scenes, the meta-learner appears to have inferred that these parameters are good enough during initialization and should not be optimized.

In Fig. 20, we further analyze the interactions between parameter updates. For the combination of scales and rotations (quats), both Adam and L2S$^{\mathbf{S}}$ behave additively, as the combined trend roughly mirrors the sum of their individual contributions. However, for means and scales in L2S$^{\mathbf{S}}$, although updating only scales degrades performance from an early iteration, jointly updating means and scales continues to improve results throughout training. This suggests a dependency between these updates in L2S$^{\mathbf{S}}$ that is not present in standard optimizers.

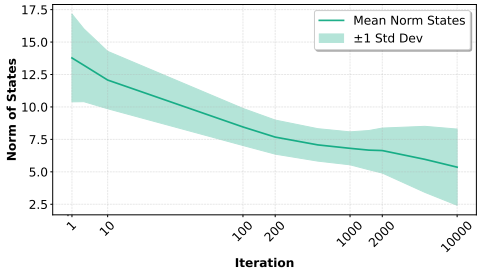
In Fig. 21, we illustrate the effect of swapping update steps between Adam and L2S$^{\mathbf{S}}$. The results show that L2S$^{\mathbf{S}}$ provides more effective updates for the means and shN parameters. Replacing Adam's updates with L2S$^{\mathbf{S}}$-style updates for these parameters consistently improves Adam's performance, whereas applying Adam's updates within L2S$^{\mathbf{S}}$ leads to degradation. In contrast, the behavior of the scale parameters is less clear: transferring their updates between the two algorithms deteriorates performance in both directions, suggesting that neither method has a clear advantage for this parameter type. For the remaining parameters, swapping updates produces no change, indicating that Adam and L2S$^{\mathbf{S}}$ behave similarly for those components.



(a) Ours: Update norms

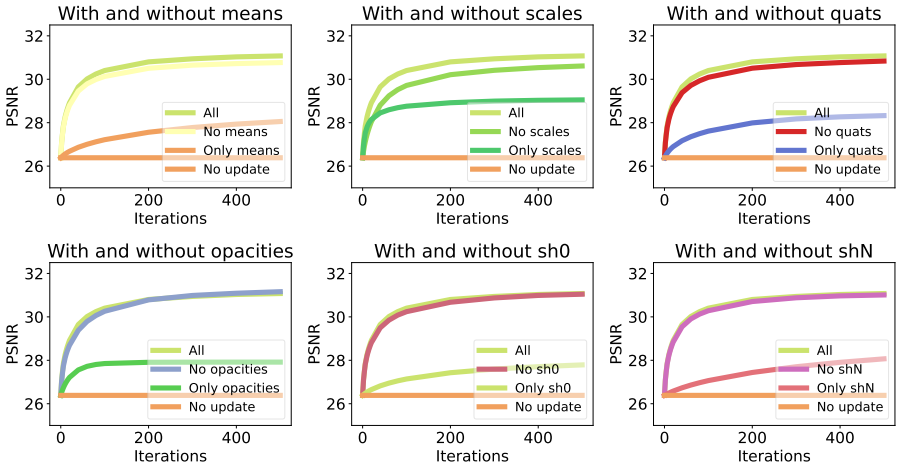


(b) 3DGS: Update norms

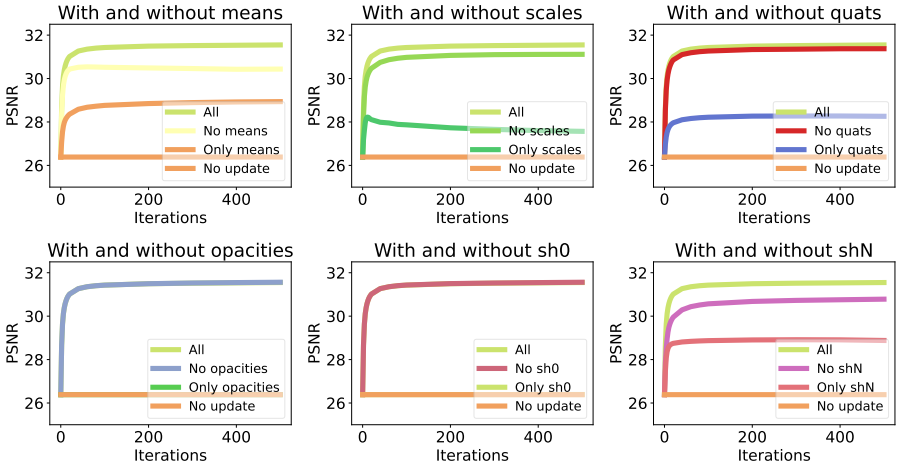


(c) Ours: Latent state norms

Fig. 18: Optimization Dynamics and State Norms. (a, b) Gaussian update norms for L2S$^{\mathbf{S}}$ and 3DGS. At each iteration, we report the update norm for each parameter group, averaged across 10 scenes from the DL3DV test set (8 views, 256 × 448). **(c)** Corresponding latent state norms for L2S$^{\mathbf{S}}$ averaged across all Gaussians and scenes. All values are computed in the sparse, low-resolution setting.

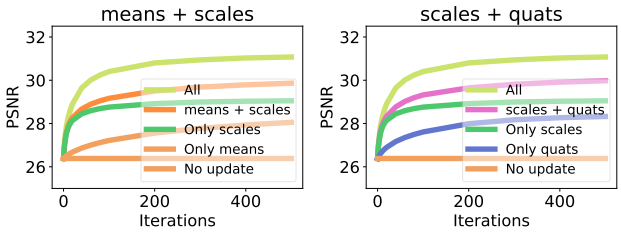


(a) Adam: per-parameter update analysis.

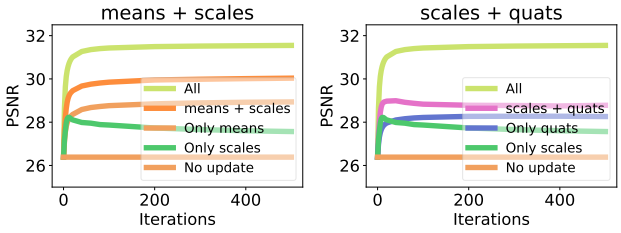


(b) Learn2Splat: per-parameter update analysis.

Fig. 19: Per-parameter updates contributions. Analysis of the contribution of each parameter in Adam optimization (top) and L2S$^{\mathbf{S}}$ optimization (bottom). Each plot shows four configurations: (1) full optimization (all parameters updated), (2) updates applied to all parameters except the selected one, (3) updates applied only to the selected parameter, and (4) frozen parameters (no updates). Results are computed over 10 scenes from the DL3DV test set in the sparse low-resolution setting (8 views, 256×448 resolution).



(a) Adam: contribution of the combination of parameters.



(b) Learn2Splat: contribution of the combination of parameters.

Fig. 20: Joint parameters updates contributions. Analysis of the joint contribution of two parameters in Adam (top) and L2S$^{\mathbf{S}}$ (bottom). Each plot includes five configurations: (1) full optimization with all parameters updated, (2) updates applied only to the selected parameter pair, (3-4) updates applied to just one of the two parameters, and (5) all parameters frozen. For Adam, the results suggest (as expected) that parameters do not influence each other. In contrast, for L2S$^{\mathbf{S}}$, the combination of means and scales shows a positive interaction between the two parameters. Results are computed over 10 scenes from the DL3DV test set in the sparse low-resolution setting (8 views, 256×448 resolution).

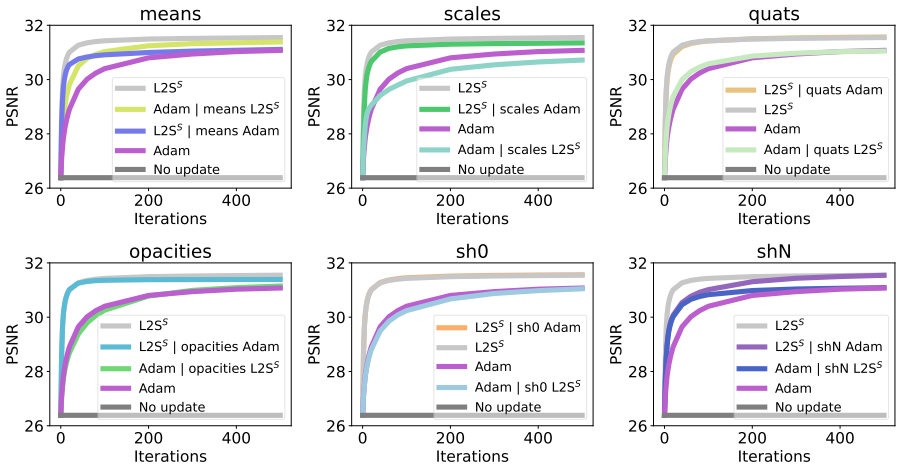


Fig. 21: Per-parameter updates swap. Analysis of swapping parameter updates between Adam and L2S$^{\mathbf{S}}$. Each plot shows five configurations: (1) full optimization with L2S$^{\mathbf{S}}$, (2) L2S$^{\mathbf{S}}$ with one parameter updated using Adam, (3) Adam with one parameter updated using L2S$^{\mathbf{S}}$, (4) full optimization with Adam, and (5) all parameters frozen. The results indicate that the updates for the means and shN are better handled by L2S$^{\mathbf{S}}$: incorporating L2S$^{\mathbf{S}}$ updates into Adam improves Adam's performance, whereas replacing L2S$^{\mathbf{S}}$ updates with Adam's versions degrades performance. For the scales, the evidence is mixed, as transferring this update in either direction worsens results. For the remaining parameters, swapping updates appears to make little difference. Results are computed over 10 scenes from the DL3DV test set in the sparse low-resolution setting (8 views, 256×448 resolution).

Symbol	Description
3D Gaussian representation	
$\boldsymbol{\mathcal{G}} = \{\boldsymbol{\mathcal{G}}_m\}_{m=1}^{G}$	Set of G 3D Gaussians, also referred to as a matrix $\boldsymbol{\mathcal{G}} \in \mathbb{R}^{G\times p}$
$\boldsymbol{\mathcal{G}}_m = \{\mathbf{p}_m, \mathbf{q}_m, \mathbf{s}_m, \alpha_m, \mathbf{SH}_m\}$	Parameters of Gaussian m, also referred to as a vector $\boldsymbol{\mathcal{G}}_m \in \mathbb{R}^p$
$\mathbf{p}_m \in \mathbb{R}^3$	3D mean (center) of Gaussian m
$\mathbf{q}_m \in \mathbb{R}^4$	Rotation (quaternion) of Gaussian m
$\mathbf{s}_m \in \mathbb{R}^3$	Scale vector of Gaussian m
$\alpha_m \in [0,1]$	Opacity of Gaussian m
$\mathbf{SH}_m \in \mathbb{R}^{d\times 3}$	Spherical harmonics coefficients of Gaussian m
p	Number of parameters per Gaussian. In our case, $p = 59$
G	Total number of Gaussians
Scene and rendering	
$\mathcal{V}$	Set of N views $\mathcal{V}_i$
$\mathcal{V}_i$	View i, including intrinsics, rotation, and translation $(\mathbf{K}_i, \mathbf{R}_i, \mathbf{t}_i)$
$\tilde{\mathbf{I}}_i(\boldsymbol{\mathcal{G}})$	Rendered image given Gaussians $\boldsymbol{\mathcal{G}}$ and viewpoint $\mathcal{V}_i$
$\mathcal{L}(\mathbf{I}_i, \tilde{\mathbf{I}}_i(\boldsymbol{\mathcal{G}}))$	Reconstruction loss for view $\mathcal{V}_i$ given the Gaussians $\boldsymbol{\mathcal{G}}$
Optimization	
t	Inner optimization step
$\boldsymbol{\mathcal{G}}_t$	Gaussian set at optimization step t
$\nabla_{\boldsymbol{\mathcal{G}}_t} = \nabla_{\boldsymbol{\mathcal{G}}_t}\mathcal{L}_{\text{inner}}(\mathbf{I}_i, \tilde{\mathbf{I}}_i(\boldsymbol{\mathcal{G}}_t))$	Gradient of the inner loss w.r.t. the Gaussian parameters at t
$f(\cdot)$	Standard optimizer (e.g., SGD, Adam)
$f_{\boldsymbol{\theta}}(\cdot)$	Learned optimizer parameterized by weights $\boldsymbol{\theta}$
$\boldsymbol{\theta}$	Parameters of the learned optimizer network
η_t	Learning rate or step size at iteration t
$\mathbf{m}_t, \mathbf{v}_t$	First and second moment estimates in Adam
β_1, β_2	Exponential decay rates for moment estimation
ϵ	Numerical stability constant in Adam
Meta-learning training	
t_{meta}	Meta optimization step
$\mathcal{V}^j$	Scene j sampled from the training dataset
$\boldsymbol{\mathcal{G}}_t^j(\boldsymbol{\theta}_{t_{\text{meta}}})$	State of Gaussians for scene j after t updates using the learned optimizer $\boldsymbol{\theta}_{t_{\text{meta}}}$ at t_{meta}
$\mathbf{I}^j$	Ground-truth RGB images of a set of views from scene j
$\tilde{\mathbf{I}}^j(\boldsymbol{\mathcal{G}}_t^j(\boldsymbol{\theta}_{t_{\text{meta}}}))$	Rendering of a set of images from scene j given Gaussians $\boldsymbol{\mathcal{G}}_t^j$
$\mathcal{L}_{t_{\text{meta}}}(\mathbf{I}^j, \tilde{\mathbf{I}}^j(\boldsymbol{\mathcal{G}}_{t+\tau}^j(\boldsymbol{\theta}_{t_{\text{meta}}}))$	Meta loss after τ unrolled steps
$\nabla_{\boldsymbol{\theta}_{t_{\text{meta}}}} = \nabla_{\boldsymbol{\theta}_{t_{\text{meta}}}}\mathcal{L}_{t_{\text{meta}}}$	Gradient of the meta-loss w.r.t. the learned optimizer weights
τ	Number of unrolled inner steps per meta-iteration
V	Total number of training scenes
Model architecture	
$\nabla_{\boldsymbol{\mathcal{G}}_t} \in \mathbb{R}^{G\times 59}$	Adam-style per-Gaussian gradients at iteration t
$\boldsymbol{\mathcal{G}}_t \in \mathbb{R}^{G\times 59}$	Gaussian parameters at iteration t
$\mathbf{s}_t \in \mathbb{R}^{G\times 256}$	Latent states of Gaussians at iteration t
$\mathbf{s}_{t+1}$	Updated latent states before scaling
$\boldsymbol{\rho}_{\mathbf{s}} \in \mathbb{R}^G$	Predicted per-Gaussian scaling coefficients for latent states
$\tilde{\mathbf{s}}_{t+1}$	Scaled latent states after applying $\boldsymbol{\rho}_{\mathbf{s}}$
$\mathbf{O}_{\mathbf{g}_t} \in \mathbb{R}^{G\times 60}$	Raw parameter updates predicted by the network
$\bar{\Delta}_{\mathbf{g}_t} \in \mathbb{R}^{G\times 59}$	Direction of parameter updates (unit-length)
$\boldsymbol{\rho}_{\Delta_t} \in \mathbb{R}^G$	Learned per-Gaussian update magnitude
$\Delta_{\boldsymbol{\mathcal{G}}_t}$	Final Gaussian parameter updates
Checkpoint buffer and training dynamics	
p_{buffer}	Probability of sampling a scene state from the checkpoint buffer
p_{push}	Probability of storing a newly optimized scene into the buffer
$p_{\text{push-back}}$	Probability of re-storing a previously sampled scene
$\mathcal{B}$	Checkpoint buffer containing intermediate Gaussian states
τ_a	Number of optimizer rollout inner steps before storing to checkpoint buffer

Table 4: Summary of notations used in this paper.